Defect generation and deconfinement on corrugated topographies

Vincenzo Vitelli and David R. Nelson
Department of Physics, Harvard University, Cambridge, Massachusetts 02138, USA
(Received 15 June 2004; published 16 November 2004)

We investigate topography-driven generation of defects in liquid crystal films coating frozen surfaces of spatially varying Gaussian curvature whose topology does not automatically require defects in the ground state. We study in particular disclination-unbinding transitions with increasing aspect ratio for a surface shaped as a Gaussian bump with a hexatic phase draped over it. The instability of a smooth ground state texture to the generation of a *single* defect is also discussed. Free boundary conditions for a single bump are considered as well as periodic arrays of bumps. Finally, we argue that defects on a bump encircled by an aligning wall undergo sharp deconfinement transitions as the aspect ratio of the surface is lowered.

DOI: 10.1103/PhysRevE.70.051105 PACS number(s): 05.40.−a, 61.30.−v, 68.60.−p

I. INTRODUCTION

The melting of a two-dimensional crystal can occur continuously via two second order topological phase transitions characterized by the successive unbinding of dislocation and disclination pairs. At low temperatures, dislocations are suppressed due to their large energy cost, but as the temperature is increased, the entropy gained by creating defects overcomes their cost in elastic energy and dislocation unbinding occurs to reduces the overall free energy of the system [1–3]. The quasi-long-range order of the crystal is thus destroyed leading to a hexatic phase that still preserves quasi-long-range orientational order. This phase can be characterized by a complex order parameter with sixfold symmetry. As the temperature is increased still further, an additional disclination-unbinding transition occurs and the hexatic order is finally lost in an isotropic liquid phase [1].

Experimental evidence for hexatic order and defect-mediated melting has been obtained in systems as diverse as free standing liquid crystal films [4], Langmuir-Blodgett surfactant monolayers [5], two-dimensional magnetic bubble arrays [6], electrons trapped on the surface of liquid helium [7–9], two-dimensional colloidal crystals [10,11], and self-assembled block copolymers [12].

The unbinding of defects in the plane is entropically driven and at low temperature defects are tightly bound. By contrast, on surfaces with nonzero (integrated) Gaussian curvature, excess defects *must* be present even at very low temperatures. The theory of topological defects in ordered phases confined to frozen topographies with positive or negative Gaussian curvature has been investigated previously; see, e.g., [13–15]. As a general rule, regions of positive or negative curvature (valleys, hills, or saddles) lead to unpaired disclinations in the ground state, possibly screened by clouds of dislocations. These clouds can in turn condense into grain boundaries at low temperature. The predictions of recent studies of crystalline order on a sphere [16] have been confirmed in elegant studies of colloidal particles packed on the surface of water droplets in oil [17]. Investigations of the physics of defects in curved spaces have also been carried out for fluctuating geometries [18–21]. The dynamics of hexatic order on fluctuating spherical interfaces was studied in Ref. [22]. Quenched *random* topographies in the limit of small deviations from flatness were investigated in Ref. [13].

In the present work, we investigate topography-driven generation of defects on simple frozen surfaces with spatially varying Gaussian curvature whose topology does *not* automatically enforce their presence in the ground state. We study in particular a two-dimensional "bump" with a Gaussian shape and dimension large compared to the particle spacing. For such a hilly landscape, flat at infinity, the *geometric* control parameter is an aspect ratio given by the bump height divided by its spatial extent. Consider a hexatic phase draped over such a bump. For small bumps, the ideal hexatic texture is distorted, but there are no defects in the ground state. As the aspect ratio is increased, we find that disclination pairs progressively unbind at $T=0$ in a sequence of transitions occurring at critical values of the aspect ratio. The defects subsequently position themselves to partially screen the Gaussian curvature. For bumps embedded in surfaces of sufficiently small spatial extent, a second instability of the smooth ground state needs to be considered. In this case, the energy stored in the field can be lowered by generating a *single* positive defect at the center of the bump. Novel effects also arise when the hilly surface is encircled by an aligning circular wall that ensures a 2π rotation of the orientational order in the ground state. In this case, some of the positive defects required to match the curvature of the boundary are confined to a hemispherical cup centered on the bump, provided the aspect ratio α is larger than a critical value α_D. When α is lowered below α_D, the positive defects originally "trapped" in the hemispherical cup start undergoing a series of sharp "deconfinement transitions," as they progressively migrate to new equilibrium positions dictated by boundary conditions and the finite system size. We also suggest possible ground states for periodic arrays of bumps, like those on the bottom of an egg carton.

A natural arena to experimentally study the interplay between geometry and defects is provided by thin copolymer films on SiO_2 patterned substrates [23]. Flat space experiments by Segalman *et al.* have already demonstrated that spherical domains in block copolymer films form hexatic phases [12].

Our results for hexatics on frozen topographies also apply to other *XY*-like models, as might be appropriate for tilted surface-active molecules on curved substrates with interac-

tions which favor alignment. The results are relevant as well to twofold nematic order on frozen topographies. In both cases, we expect qualitatively similar defect-unbinding transitions, although the equivalence becomes more exact in the one-Frank-constant approximation [24]. Related results have been obtained recently for order on a torus [25]. Even though the *integrated* Gaussian curvature vanishes, defects appear in the ground state in the limit of fat torii, unless the number of degrees of freedom is very large.

The outline of this paper is as follows. In Sec. II, the relevant mathematical formalism is introduced and used to highlight similarities and differences between defects on surfaces of varying curvature and electrostatic charges in a nonuniform background charge distribution in flat space. As an example, we calculate the distorted, but defect-free, ground state texture of a hexatic confined to a surface shaped as a "Gaussian bump" for aspect ratios below the first disclination-unbinding instability. In Sec. III, we investigate curvature-induced defect formation for an isolated bump and a periodic array of bumps. In Sec. IV, defect deconfinement is discussed and in Sec. V various experimental issues related to our analysis are highlighted along with some directions for future work. The development of the mathematical formalism is largely relegated to appendixes. In Appendix A the Green's function for the covariant Laplacian is derived by means of conformal transformations. In Appendix B, we introduce a geometric potential whose source is the Gaussian curvature. In Appendix C, we present the general formula for the energy of textures with defects in terms of the two functions derived in Appendixes A and B. We thus explore the existence of position-dependent defect self-interactions that arise from the varying Gaussian curvature. Finally, boundary effects are discussed in Appendix D.

II. HEXATIC ORDER ON A SURFACE

A. Electrostatic analogy

The free energy for hexatic degrees of freedom embedded in an arbitrary frozen surface can be written as

$$F = \frac{K_A}{2} \int dA\, D_\alpha n^\beta(\mathbf{u}) D^\alpha n_\beta(\mathbf{u}), \tag{1}$$

where $\mathbf{u}=\{u_1,u_2\}$ is a set of internal coordinates, $\mathbf{n}(\mathbf{u})$ is a unit vector in the tangent plane, D_α is the covariant derivative with respect to the metric of the surface, and dA is the infinitesimal surface area [18,19,21,26]. The generalization to systems with a p-fold symmetry is straightforward provided that the one-Frank-constant approximation is used and the consequences of the uniaxial coupling neglected [24]. This choice of free energy implies that the minimal energy configuration will be given locally by neighboring $\mathbf{n}(\mathbf{u})$ vectors which differ only by parallel transport. The curvature of the surface induces "frustration" in the texture. In fact, by Gauss' "theorema egregium" [27,28], tangent vectors parallel transported along a closed loop are rotated by an amount equal to the Gaussian curvature integrated over the enclosed area. On a sphere, for example, the hexatic ground state always has 12 excess disclinations as a result of this frustration [14,29]. More generally, the sum of the topological charges on any closed surface is equal to the integrated Gaussian curvature.

By introducing a local bond-angle field $\theta(\mathbf{u})$, corresponding to the angle between $\mathbf{n}(\mathbf{u})$ and an arbitrary local reference frame, we can rewrite the hexatic free energy introduced in Eq. (1) as

$$F = \frac{1}{2} K_A \int dA\, g^{\alpha\beta}(\partial_\alpha\theta - A_\alpha)(\partial_\beta\theta - A_\beta), \tag{2}$$

where $dA=d^2u\sqrt{g}$, g is the determinant of the metric tensor $g_{\alpha\beta}$, and A_β is the spin connection whose curl is the Gaussian curvature $G(\mathbf{u})$ [26,28]. The spin connection can be viewed as a "geometric vector potential." A free energy like Eq. (2) also describes the charged Cooper pairs implicit in the London theory of a superconductor well below T_C. In the superconductor analogy, the Gaussian curvature plays the role of a (spatially varying) external magnetic field. For the problem considered here, however, there are interesting new nonlinear effects associated with spatial variations in the metric.

A detailed analysis of the free energy of Eq. (2) for a bumpy surface with free and circular boundary conditions is presented in Appendixes C and D. Here we only sketch the main steps and conclusions. The free energy can be readily converted into a Coulomb gas model by using the relation

$$\gamma^{\alpha\beta}\partial_\alpha(\partial_\beta\theta - A_\beta) = s(\mathbf{u}) - G(\mathbf{u}) \equiv n(\mathbf{u}), \tag{3}$$

where $\gamma^{\alpha\beta}$ is the covariant antisymmetric tensor, $G(\mathbf{u})$ is the Gaussian curvature, and $s(\mathbf{u}) \equiv (1/\sqrt{g})\Sigma_{i=1}^{N_d} q_i \delta(\mathbf{u}-\mathbf{u}_i)$ is the disclination density with N_d defects of charge q_i at positions $\mathbf{u}_i$. The final result is an effective free energy whose basic degrees of freedom are the defects themselves [16,21]:

$$F = \frac{K_A}{2} \int dA \int dA'\, n(\mathbf{u}) \Gamma(\mathbf{u},\mathbf{u}') n(\mathbf{u}'), \tag{4}$$

where $n(\mathbf{u})$ is defined in Eq. (3). The Green's function $\Gamma(\mathbf{u},\mathbf{u}')$ is calculated (see Appendix A) by inverting the Laplacian defined on the surface

$$\Gamma(\mathbf{u},\mathbf{u}') \equiv -\left(\frac{1}{\Delta}\right)_{\mathbf{u}\mathbf{u}'}, \tag{5}$$

and we have suppressed for now defect core energy contributions which reflect the physics at microscopic length scales. Equation (4) can be understood by analogy to two-dimensional electrostatics, with the Gaussian curvature $G(\mathbf{u})$ (with sign reversed) playing the role of a nonuniform background charge distribution and the topological defects appearing as pointlike sources with electrostatic charges equal to their topological charge q_i. As a result, the defects tend to position themselves so that the Gaussian curvature is screened: the positive ones on peaks and valleys and the negative ones on the saddles of the surface. However, this analogy does neglect position-dependent self-interactions [30], but since these are quadratic in the charge they are negligible for hexatics. Hence positive disclinations of minimal topological charge $q_i=2\pi/6$ continue to be attracted to positive curvature (see Appendix C).

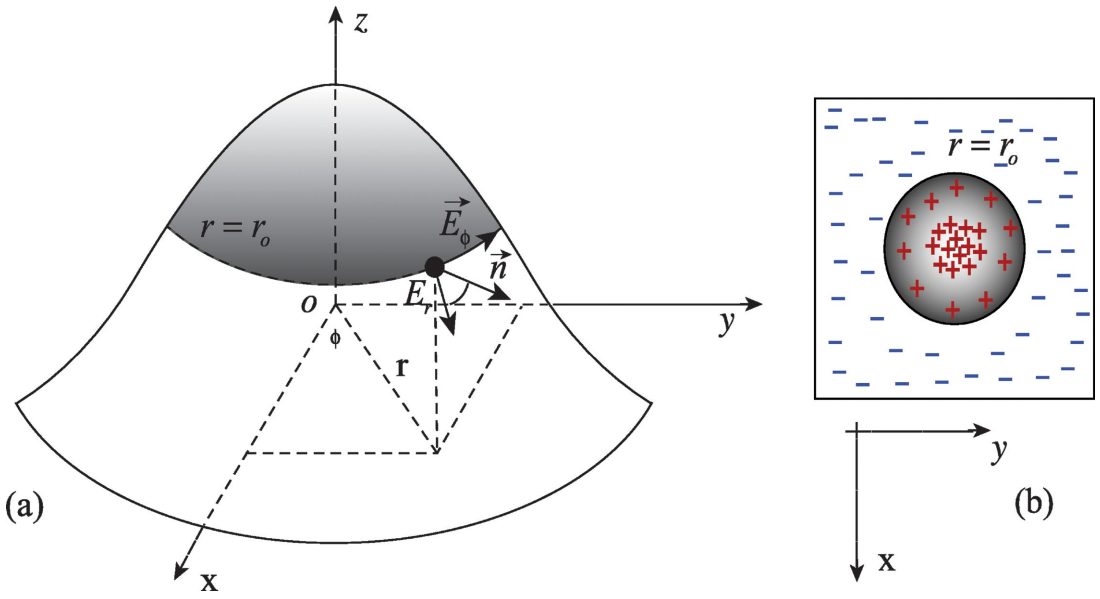

FIG. 1. (Color online) (a) The vector field **n** is confined to a surface shaped as a Gaussian. (b) Top view of (a) showing a schematic representation of the positive and negative Gaussian curvature as a background "charge" distribution that switches sign at $r=r_0$. Note that, according to the electrostatic analogy, a positive (negative) distribution of Gaussian curvature corresponds to negative (positive) topological charge density.

More generally, we can consider p-fold symmetric order parameters with minimum charge defects $\pm 2\pi/p$. The case $p=1$ corresponds to tilt order of absorbed molecules and $p=2$ describes two-dimensional (2D) nematics. The cases $p=4$ and $p=6$ describe tetradic and hexatic phases, respectively [29]. Strictly speaking, Eq. (1) describes only the cases $p=1$ and $p=2$ in the one-Frank-constant approximation [24]. Most of our discussion focuses on topography-driven transitions on a model surface shaped like a bell curve or "Gaussian bump" (see Fig. 1), but the same mathematical approach can be readily carried over to study arbitrary surfaces of revolution that are topologically equivalent to the plane. Furthermore, we do not expect the results of this analysis to depend qualitatively on the azimuthal symmetry of the surface, which is assumed purely for reasons of mathematical convenience.

Points on our model surface embedded in three-dimensional Euclidean space are specified by a three-dimensional vector $\mathbf{R}(r,\phi)$ given by

$$\mathbf{R}(r,\phi) = \begin{pmatrix} r\cos\phi \\ r\sin\phi \\ h\exp(-r^2/2r_0^2) \end{pmatrix}, \tag{6}$$

where r and ϕ are plane polar coordinates in the xy plane of Fig. 1. It is useful to characterize the deviation of the bump from a plane in terms of a dimensionless aspect ratio

$$\alpha \equiv \frac{h}{r_0}. \tag{7}$$

The two orthogonal tangent vectors $\mathbf{t}_r \equiv \partial\mathbf{R}/\partial r$ and $\mathbf{t}_\phi \equiv \partial\mathbf{R}/\partial\phi$ can be normalized to define the vierbein (orthonormal basis vectors) $\mathbf{E}_r$ and $\mathbf{E}_\phi$, respectively. The components of the spin connection introduced in Eq. (2) are given by $\mathbf{A}_\alpha = \mathbf{E}_r \cdot \partial_\alpha \mathbf{E}_\phi$ [26,28]. This leads to a vanishing radial component A_r and

$$A_\phi = -\frac{1}{\sqrt{l(r)}}, \tag{8}$$

where the important α-dependent function $l(r)$ (see Fig. 2) is defined by

$$l(r) \equiv 1 + \frac{\alpha^2 r^2}{r_0^2}\exp\left(-\frac{r^2}{r_0^2}\right), \tag{9}$$

and it is equal to the radial component of the diagonal metric tensor $g_{\alpha\beta}$,

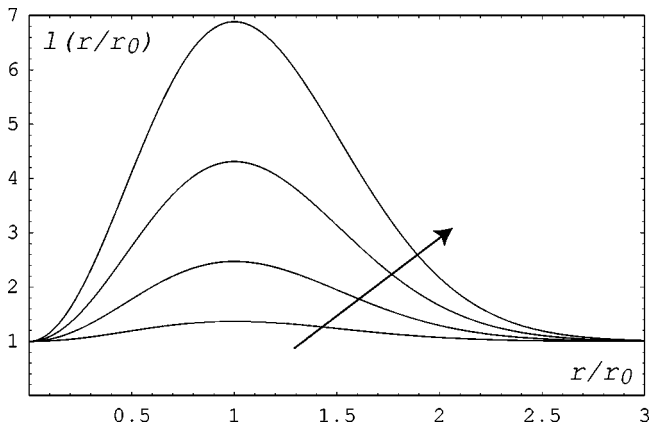

FIG. 2. Plot of $l(r/r_0)$ as a function of the dimensionless radial coordinate r/r_0 for $\alpha=1,2,3,4$. The arrow is oriented in the direction of increasing α.

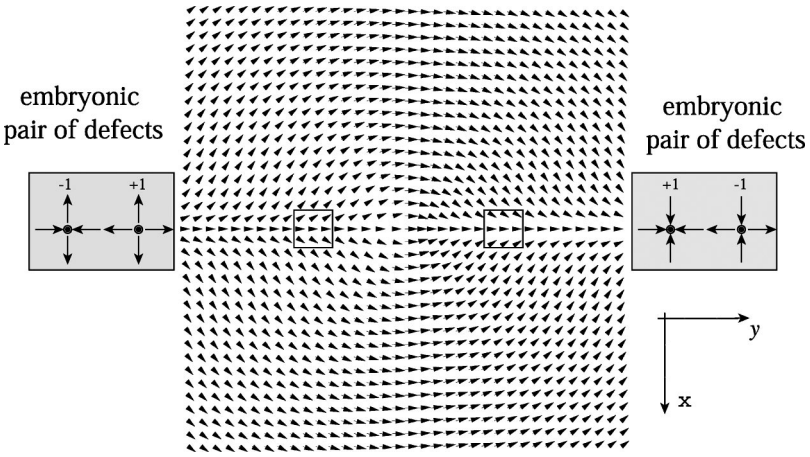

FIG. 3. Projected ground state texture for an *XY* model on the bump, with the boundary condition that the vector field is parallel to the *y* axis at infinity. The two insets show the defect pairs suggested by two regions of large frustration, which lie close to a circle of radius r_0.

$$g_{\alpha\beta} = \begin{pmatrix} l(r) & 0 \\ 0 & r^2 \end{pmatrix}. \tag{10}$$

Note that the $g_{\phi\phi}$ entry is equal to the flat space result r^2 in polar coordinates while $g_{rr}=l(r)$ is modified in a way that depends on α but tends to the plane result $g_{rr}=1$ for small and large r, as illustrated in Fig. 2.

The Gaussian curvature for the bump is readily found from the eigenvalues of the second fundamental form [31],

$$G_\alpha(r) = \frac{\alpha^2 e^{-r^2/r_0^2}}{r_0^2 l(r)^2}\left(1 - \frac{r^2}{r_0^2}\right). \tag{11}$$

Note that α controls the order of magnitude of $G(r)$ and that $G(r)$ changes sign at $r=r_0$ [see Fig. 1(b)]. The integrated Gaussian curvature $\Delta G(r)$ inside a cup of radius r centered on the bump is

$$\Delta G(r) = 2\pi\left(1 - \frac{1}{\sqrt{l(r)}}\right), \tag{12}$$

which vanishes as $r\to\infty$. Equation (12) also shows that the positive Gaussian curvature enclosed within the radius r_0 (see Fig. 1) approaches 2π for $\alpha \gg 1$, half the integrated Gaussian curvature of a sphere.

B. Defect-free texture

For small values of the aspect ratio α, the minimal energy texture for the hexatic will be free of defects. The ground state configuration $\theta_0(\mathbf{u})$ satisfies the differential equation

$$D_\alpha D^\alpha \theta_0 - D^\alpha A_\alpha = 0, \tag{13}$$

which results from minimizing the free energy in Eq. (2) with respect to the field $\theta(\mathbf{u})$ for fixed A_α. When expressed in terms of the coordinates in Eq. (6), the solution of Eq. (13) reads

$$\theta_0(\mathbf{u}) = -\phi + c, \tag{14}$$

where c is an arbitrary constant. The smooth ground state texture is thus obtained if the director $\mathbf{n}$ forms an angle $\theta_0(\mathbf{u})=-\phi+c$ with respect to the spatially varying basis vector $\mathbf{E}_r$. Note that a solution of the form $\theta_0(\mathbf{u})=c$ represents a defect of charge $q=2\pi$ in this "rotating" system of coordinates.

As an illustration, consider the projection on the plane of the minimal energy texture of an *XY* model ($p=1$) as shown in Fig. 3. The arrows represent the orientation of tilted molecules on this surface in the one-Frank-constant approximation. The field clearly displays strong frustration along a direction determined by the choice of the constant c in Eq. (14). If the bump is positioned within two very distant walls parallel to the *y* axis which impose tangential boundary conditions on the molecular tilts, the "preferred" direction will be along $\hat{y}$.[1] The texture displayed in Fig. 3 can be interpreted as resulting from embryonic pairs of defect dipoles along the line $x=0$. The distortion energy F_0 of this ground state is given by

$$F_0 = \frac{1}{2}K_A \int dA\, g^{\alpha\beta}(\partial_\alpha\theta_0 - A_\alpha)(\partial_\beta\theta_0 - A_\beta). \tag{15}$$

This expression can be evaluated for an infinitely large system by using Eq. (14) and the explicit form of the spin connection derived in Sec. II A, with the result

$$F_0 = \pi K_A \int_0^\infty dr \frac{[1-\sqrt{l(r)}]^2}{r\sqrt{l(r)}}. \tag{16}$$

It follows from Eq. (16) that the ground state energy is a monotonically increasing function of the aspect ratio, proportional to α^4 for small α. As we shall see, for large enough α, it can be energetically preferable to reduce this energy by introducing defect pairs into the texture. It is convenient to rewrite Eq. (15) in terms of the Gaussian curvature $G(r)$ and the Green's function $\Gamma(\mathbf{u},\mathbf{u}')$ discussed in Appendix A [26]

[1] In case *distant* walls are present, the free solution of Eq. (14) is slightly modified to account for the new boundary conditions. This is accomplished by the method of images or conformal transformations [32].

$$F_0 = \frac{K_A}{2} \int dA \int dA' G(\mathbf{u}) \Gamma(\mathbf{u},\mathbf{u}') G(\mathbf{u}'). \tag{17}$$

This result is what one obtains by setting all $q_i = 0$ in Eq. (4). The details of the mathematical derivation are relegated to Appendix C.

Although this result correctly represents the zero-temperature limit of the vector model, corrections may be appropriate to describe the physics of ordered phases at finite temperature. "Spin-wave" excitations (i.e., quadratic fluctuations of the order parameter about the ground state texture) can be accounted for by integrating out the longitudinal fluctuations $\theta'(\mathbf{u})$ around the ground state configuration $\theta_0(\mathbf{u})$. By letting $\theta = \theta_0 + \theta'$ in Eq. (2) and using Eq. (3) we obtain [18,21]

$$F = F_0 + \frac{1}{2} K_A \int dA\, g^{\alpha\beta} \partial_\alpha \theta' \partial_\beta \theta'. \tag{18}$$

The longitudinal variable $\theta'(\mathbf{u})$ appears only quadratically in F and the trace over $\theta'(\mathbf{u})$ can be explicitly performed with the result [33]

$$\int \mathcal{D}\theta' \exp\left(- \frac{\beta K_A}{2} \int dA\, g^{\alpha\beta} \partial_\alpha \theta' \partial_\beta \theta' \right) = e^{-\beta F_L}, \tag{19}$$

where F_L is the Liouville action,

$$\beta F_L = c \int dA - \frac{K_A}{24} \int dA \int dA' G(\mathbf{u}) \Gamma(\mathbf{u},\mathbf{u}') G(\mathbf{u}'). \tag{20}$$

The first term in this expression is a constant proportional to the fixed surface area of the frozen topography and will be suppressed in what follows. The remaining term causes a shift in the coupling constant appearing in Eq. (17) from K_A to $K_A' = K_A - k_B T / 12\pi$ [18,21]. This "entropic" correction to the coupling constant K_A at finite temperature also arises when defects are present.

The energy in Eq. (17) represents an intrinsic, irreducible energy cost of geometric frustration for textures without defects. As we shall see, defects can reduce this frustration. However, for small values of α the energy cost of this frustration will still be lower than the core energies associated with the creation of the unbound defects and the work necessary to tear them apart.

C. Energetics of defect pairs on a Gaussian bump

A quantitative understanding of the energetics of defects on a fixed topography is essential to calculate the critical value(s) of the aspect ratio above which defect unbinding becomes energetically favorable. The first step is to calculate the Green's function $\Gamma(\mathbf{u},\mathbf{u}')$ that governs the "Coulombic" interaction among defects and between each defect and the Gaussian curvature. The inversion of the curved space Laplacian can be more easily accomplished by employing a set of "isothermal coordinates," such that the resulting Green's function reduces to the familiar logarithm of two-dimensional electrostatics. As shown in Appendix A the final result in terms of the original polar coordinates reads

$$\Gamma(\mathbf{u},\mathbf{u}') = - \frac{1}{4\pi} \ln[\Re(r)^2 + \Re(r')^2 - 2\Re(r)\Re(r')\cos(\phi - \phi')] + c, \tag{21}$$

where the function $\Re(r)$ can be thought of as a radial coordinate in the conformal plane resulting from adopting an isothermal set of coordinates (see Appendix A)

$$\Re(r) = r \exp\left(- \int_r^\infty \frac{dr'}{r'} [\sqrt{l(r')} - 1] \right), \tag{22}$$

and $l(r)$ is the α-dependent function introduced in Eq. (9). The constant c depends on the physics at short distances, which is discussed in Appendix A.

The Green's function in Eq. (21) corresponds to free boundary conditions at infinity and preserves the cylindrical symmetry of the metric. It differs from the familiar result in flat space by a nonlinear radial stretch corresponding to a smooth deformation of the bump into a flat disk. This Green's function determines an attractive interaction for the defect-dipole pair. However, the Gaussian curvature of the bump also generates a geometric potential that tries to pull the disclination dipole apart. This geometric interaction arises by combining cross terms between $s(\mathbf{u})$ and $G(\mathbf{u})$ in Eq. (4) with the position-dependent self-interactions derived in Appendix C. The resulting interaction F_G between defects and the Gaussian curvature takes the simple form

$$F_G = K_A \sum_{i=1}^{N_d} q_i \left(1 - \frac{q_i}{4\pi} \right) V(\mathbf{u}_i), \tag{23}$$

where the geometrical potential $V(\mathbf{u})$ is defined as

$$V(\mathbf{u}) \equiv - \int dA\, G(\mathbf{u}') \Gamma(\mathbf{u},\mathbf{u}'). \tag{24}$$

The minus sign in front of this geometric potential ensures that defects of topological charge between zero and 4π are attracted by regions of positive Gaussian curvature [30]. For defects with a large topological charge of $q > 4\pi$, the sign of the geometric interaction F_G is reversed and defects of either sign are pushed away from the bump. This scenario does not affect the geometry-driven defect formation discussed in this paper that relies on disclinations whose charge is well below 4π. However, as a result of the position-dependent self-interactions, F_G is no longer symmetric under the change $q \to -q$, as one would expect on the basis of the electrostatic analogy. The effect of this asymmetry is small for hexatic order but it increase for liquid crystals with p-fold order parameter, as p decreases (see Ref. [30], and references therein).

Gauss' law generalized to curved surfaces (see Appendix B) ensures that the geometric force experienced by a defect of charge q with radial coordinate r will be determined only by the net curvature enclosed in a circle of radius r centered on the top of the bump. The resulting "electric field" is radial

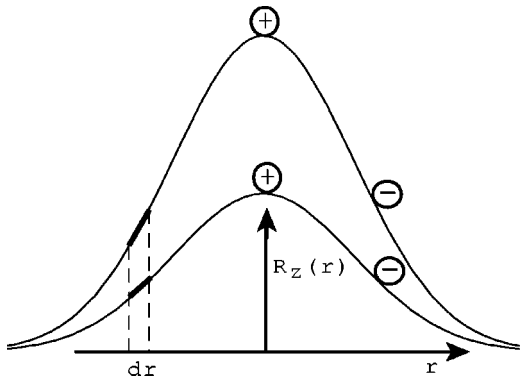

FIG. 4. Effect of changing the aspect ratio of the bump on the work needed to pull apart two oppositely charged defects. Positive and negative defects are represented by open circles with their sign printed. The line elements corresponding to the projected length *dr* for the two aspect ratios are shown.

as expected from electrostatics and is proportional to the gradient of the geometric potential, which for a Gaussian bump takes the form (see Appendix B)

$$V(r) = -\int_r^\infty \frac{dr'}{r'}[\sqrt{l(r')} - 1]. \tag{25}$$

For small values of the aspect ratio α the potential in Eq. (25) can be approximated by

$$V(r) \approx -\frac{\alpha^2 e^{-r^2/r_0^2}}{4}. \tag{26}$$

The resulting force is linear for small r (i.e., near the top of the bump) and decays like e^{-r^2/r_0^2} for $r \gg r_0$. As the aspect ratio α increases, the force generated by the curvature can overcome the attractive force binding the defect pair which varies logarithmically for short distances. As a result, oppositely charged defects that were originally tightly bound can be separated.

This argument, however, neglects another complication resulting from the curvature of the surface: as the aspect ratio is increased, the Green's function $\Gamma(\mathbf{u},\mathbf{u}')$ in Eq. (21) and hence the force binding the defects together *also* increases. We illustrate this point in Fig. 4 for the special case of a positive defect pinned right on top of the bump and a negative one free to move downhill at r. Upon invoking Eqs. (4) and (21), the potential binding the pair, $V_{pair}(r)$, can be written down exactly as

$$V_{pair}(r) = \frac{K_A q^2}{2\pi}\ln\left(\frac{r}{a}\right) + 2q^2 E_c - \frac{K_A q^2}{2\pi}\int_r^\infty \frac{dr'}{r'}[\sqrt{l(r')} - 1]. \tag{27}$$

The first term is the flat space Green's function and we have added two disclination core energies. The last term represents a "curvature correction" that has the same functional form of the geometric potential in Eq. (25), but it represents a distinct contribution to the total free energy. As discussed in Appendix B, the pair potential energy $V_{pair}(r)$ can be understood by applying a generalized Gauss' law to the bump to determine a force which is equal to $-q^2/2\pi r$. The potential follows by integrating this force along the bump with the length element $dr\sqrt{l(r)}$.

Although the force is independent of the aspect ratio, the length element grows with α (see Fig. 4), which makes the pair more energetically bound for larger values of α. A careful calculation of these effects (including the contribution associated with the position-dependent self-energies) reveals that the geometric force still overcomes the binding interaction for sufficiently large values of α.

An estimate of the critical value of α for which the dipole unbinds can be obtained by comparing the minimal free energy of the smooth frustrated field arising from Eq. (17) with the free energy in the presence of defects. The latter, as follows from Eq. (4), is composed of three contributions: the interactions among the defects, the interaction between the defects and curvature as given by Eq. (23), and the Gaussian curvature self-interaction. The latter is equal to the minimal free energy of the smooth frustrated field and is renormalized at finite temperature in the same way. (Associated with the cutoff is a microscopic core energy E_c that we expect to be *independent* of the defect position on the bump, as long as the radius of curvature is much greater than any microscopic length scale.) The remaining two contributions are not renormalized by thermally induced spin wave fluctuations [21]. As shown in Appendix C, the difference in free energy of a defected texture described by Eq. (4) relative to the defect-free result Eq. (17) can be written as

$$\frac{\Delta F(\alpha)}{K_A} = \frac{1}{2}\sum_{i=1}^{N_d}\sum_{j\neq i}^{N_d} q_i q_j \Gamma_a(r_i,\phi_i,r_j,\phi_j) + \sum_{i=1}^{N_d} q_i\left(1 - \frac{q_i}{4\pi}\right)V(r_i) + \frac{E_c}{K_A}\sum_{i=1}^{N_d} q_i^2, \tag{28}$$

where we have assumed overall charge neutrality for the defect configuration. The subscript in Γ_a indicates that a constant microscopic core radius a has been absorbed in the definition of the Green's function so that the argument of the logarithm in Eq. (21) becomes dimensionless, as in Eq. (C21),

$$\Gamma_a(r_i,\phi_i,r_j,\phi_j) = \Gamma(r_i,\phi_i,r_j,\phi_j) + \frac{1}{2\pi}\ln a. \tag{29}$$

This microscopic cutoff a corresponds to a constant core radius for each defect and it is of the order of the spacing between the microscopic degrees of freedom. The sum of microscopic core energies in the fourth term of Eq. (28) needs to be fixed phenomenologically or from models that go beyond simple elasticity theory [34]. Note that both $\Gamma_a(r_i,\phi_i,r_j,\phi_j)$ and $V(r)$ depend on α. If α becomes sufficiently large so that ΔF is less than zero, one or more disclination dipoles unbind in the hexatic phase at a sequence of critical values α_{c_i}. The analogous defects in *XY*-model textures of tilted liquid crystal molecules would be $+/-$ vortex pairs.

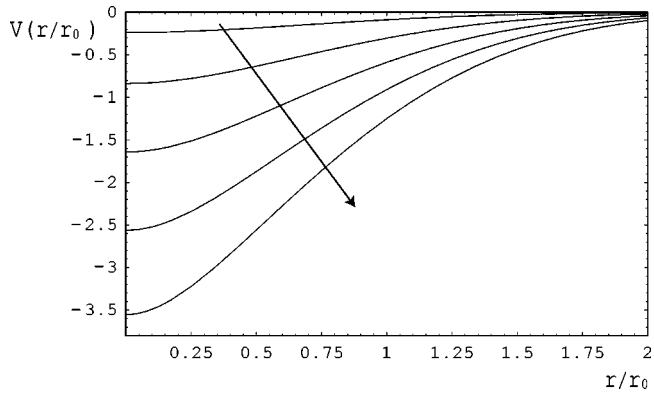

FIG. 5. Geometric potential $V(r/r_0)$ as a function of the dimensionless ratio of r and r_0 for $\alpha=1$, 2, 3, 4, 5. Note that $|V(r)| \ll |V(0)|$ for $r \gtrsim r_0$. The arrow points in the direction of increasing α.

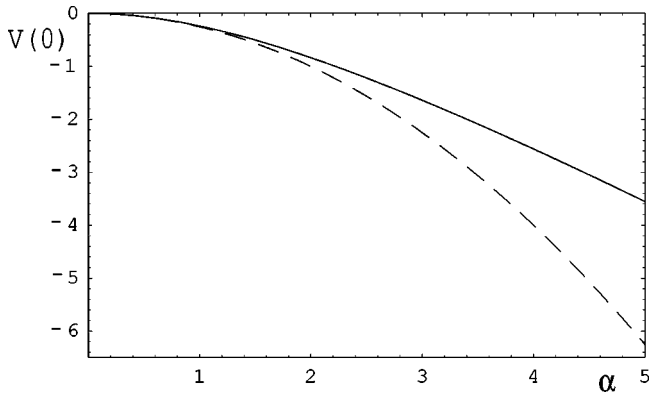

FIG. 6. Plot of the geometric potential evaluated at the center of the bump, $V(0)$, for aspect ratios α between 0 and 5. The continuous line is plotted using the exact form of $V(r)$ while the dashed line is obtained from the low-α expansion given in Eq. (26).

III. CURVATURE-INDUCED DEFECT GENERATION

A. Onset of the defect-dipole instability

If a dipole is created, say, along the line $r=r_0$ of zero Gaussian curvature, the positive disclination will be pulled toward the center by the positive curvature while the negative one will be repelled into the region of negative curvature.

The net result is a reduction of the total free energy of the order of the depth of the potential well since the logarithmic binding energy is approximately constant compared to the geometric potential. An approximate analytical treatment is obtained by assuming that the positive defect sits right at the center of the bump and the negative one at a distance of the order of r_0. The validity of this approximation scheme can be checked by numerically minimizing the energy with respect to the position of the defects, as discussed in Sec. III B. We assume charge neutrality so that the two defects have equal and opposite topological charges of magnitude q. For order parameters with a p-fold symmetry, the minimal topological charge is $q=2\pi/p$. The approximate free energy cost to generate this defect pair then follows from Eqs. (25), (27), and (28):

$$\frac{\Delta F(\alpha)}{K_A} \approx \frac{q^2}{2\pi}\left[\ln\left(\frac{r}{a}\right) + V(r)\right] + q\left(1 - \frac{q}{4\pi}\right)V(0) - q\left(1 + \frac{q}{4\pi}\right)V(r) + 2q^2\frac{E_c}{K_A}. \tag{30}$$

The internal consistency of the formalism can be checked by investigating the limit $r \to a$. As the negative defect approaches the positive one at the center of the bump, we have $V(a) \approx V(0)$ and the energy tends to the expected flat space result $2q^2E_c$.

The equilibrium position of the negative defect turns out to be for r equal to a few r_0, so the terms containing $V(r)$ in Eq. (30) can be dropped as a first approximation because $V(r)$ decays exponentially (see Fig. 5):

$$\frac{\Delta F(\alpha)}{K_A} \approx \frac{q^2}{2\pi}\ln\left(\frac{r}{a}\right) + q\left(1 - \frac{q}{4\pi}\right)V(0) + 2q^2\frac{E_c}{K_A}. \tag{31}$$

To estimate the critical value of the aspect ratio for which the first dipole unbinds, let $r \sim r_0$ and solve for α_c in Eq. (31). Because a different choice for the core energy E_c can be accounted for by rescaling the core size a in Eq. (31), the condition for unbinding is

$$|V(0)| > \frac{2q}{(4\pi - q)}\ln\left(\frac{r_0}{a'}\right) \tag{32}$$

with

$$a' = ae^{-4\pi E_c/K_A}. \tag{33}$$

If we know E_c/K_A and r_0/a, the critical aspect ratio α_c can be obtained from inspection of Fig. 6 where $V(0)$ is plotted as a function of α.

The Taylor expansion of $V(r)$ derived in Eq. (26) gives $V(0) \approx -\alpha^2/4$ to leading order in α. Inspection of Fig. 6 shows that this approximation works sufficiently well even for aspect ratios of order unity. Upon substituting for $V(0)$ into Eq. (32), we obtain an estimate of how α_c depends on r_0/a':

$$\alpha_c^2 \approx \frac{8q}{(4\pi - q)}\ln\left(\frac{r_0}{a'}\right) \approx \frac{8q}{(4\pi - q)}\left[\ln\left(\frac{r_0}{a}\right) + \frac{4\pi E_c}{K_A}\right]. \tag{34}$$

Note that a critical height $h_c=\alpha_c r_0$ for defect unbinding is predicted for fixed r_0/a' with defect charge $q=2\pi/p$ for all integer values of p. The validity of this approximate relation is tested in Sec. III B.

The continuum theory adopted here is valid in the limit $r_0 \gg a$. If E_c can be neglected compared to K_A, the defect-unbinding instability is triggered when the energy gain derived from letting the defects screen the Gaussian curvature [approximately given by $qV(0)$] overcomes the work needed to pull them apart a distance r_0. This work, of order $(q^2/2\pi)\ln(r_0/a)$, increases very slowly with large r_0/a, hence the continuum approximation can be satisfied while

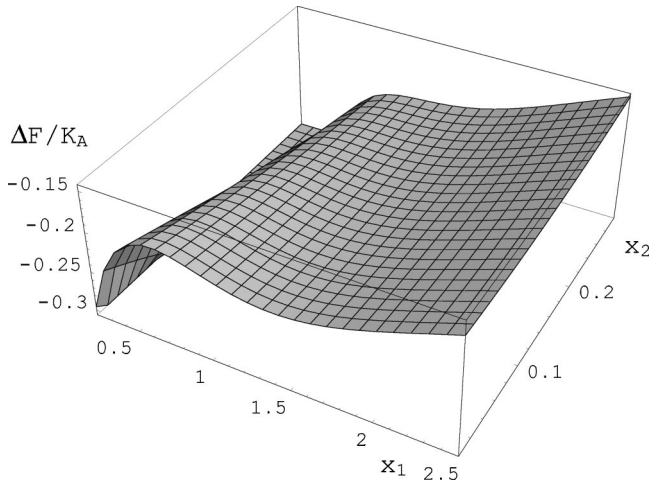

FIG. 7. Plot of $\Delta F/K_A$ versus x_1 and x_2, the positions of the negative and positive defects, respectively, in units of r_0, for $\alpha = 1.2$. A constant energy offset equal to $-(q^2/2\pi)\ln(r_0/a')$ has been neglected. The metastable minimum at $x_1 \simeq 1.3r_0$ and $x_2 \simeq 0.2r_0$ corresponds to an unbound pair [see Fig. 8(a)]. As α is decreased further the energy barrier that separates this minimum from the smooth texture solution (corresponding to x_1 approaching x_2) disappears and the two opposite defects annihilate.

keeping the work finite. Note that the result does not depend on the size of the system R because we assume overall disclination charge neutrality and the assumption that $R \gg r_0$. In this limit, boundary effects can be ignored provided that they do not impose a topological constraint on the phase of the order parameter. An aligning outer wall in a circular hexatic sample, for example, would force the bond-angle field to rotate by 2π, leading to six defects in the ground state even in flat space. The interesting physics which results is addressed in Sec. IV.

B. Numerical investigation of defect-unbinding transitions

The disclination-unbinding transitions can be investigated more quantitatively by minimizing numerically $\Delta F(\alpha)$ in Eq. (28) with respect to the positions of the defects. The aspect ratio above which $\Delta F(\alpha)$ becomes negative corresponds to the threshold value α_c (analogous to a first order transition) for which the singular field is energetically favored with respect to the smooth texture of Fig. 3. We emphasize that the energy landscape can have two minima. The first occurs when two oppositely charged defects form a closely bound dipole (with separation of the order of the cutoff a) and hence annihilate each other leaving a smooth texture. The second minimum corresponds to an unbound pair (with separation of a few r_0) and it disappears when the geometric force is too weak to overcome the binding force of the pair. This scenario occurs for a *finite* value of α characteristic of the geometry of the substrate above which the formation of an unbound dipole is possible, albeit energetically unfavored (see Fig. 7).

As α is increased above α_c, the smooth-texture minimum becomes metastable and the unbinding of a defect pair is the most likely scenario.

It is useful to parametrize $\Delta F(\alpha)$ in terms of the dimensionless radial coordinates $\overline{r_i} \equiv r_i/r_0$. The geometric potential is defined in Eq. (A9) as a function of $\overline{r_i}$, $V(r) \equiv \tilde{V}_\alpha(r/r_0)$, where

$$\tilde{V}_\alpha(x) = -\int_x^\infty \frac{dy}{y}\left[\sqrt{1+\alpha^2 y^2 \exp(-y^2)} - 1\right]. \tag{35}$$

In order to write the defect-defect interaction in terms of the dimensionless radial coordinate $\overline{r_i}$, we introduce a new function $\tilde{\Re}(\overline{r_i})$ defined by

$$\tilde{\Re}(\overline{r_i}) \equiv \frac{r_i}{r_0}\exp[V(r_i)] = \frac{r_i}{r_0}\exp\left[\tilde{V}_\alpha\left(\frac{r_i}{r_0}\right)\right] = \frac{\Re(r_i)}{r_0}, \tag{36}$$

where Eq. (A8) was used in the last step. We can now transform $\Gamma_a(\overline{r_i}, \phi_i, \overline{r_j}, \phi_j)$ by eliminating $\Re(r_i)$ in favor of $\tilde{\Re}(\overline{r_i})$. Thus we have using Eqs. (C21) and (A12)

$$-\sum_{j\neq i}^{N_d} q_i q_j \Gamma_a(r_i, \phi_i, r_j, \phi_j) = -\sum_{j\neq i}^{N_d} q_i q_j \Gamma(\overline{r_i}, \phi_i, \overline{r_j}, \phi_j) + \frac{1}{2\pi}\sum_{i=1}^{N_d} q_i^2 \ln\left(\frac{r_0}{a}\right), \tag{37}$$

where we have exploited charge neutrality and Eq. (C22). The free energy minimized with respect to the positions of the defects, $\min[\Delta F/K_A]$, can now be written, according to Eq. (28), as

$$\min\left[\frac{\Delta F}{K_A}\right] = f(\alpha) + \frac{1}{4\pi}\sum_{i=1}^{N_d} q_i^2 \ln\left(\frac{r_0}{a'}\right), \tag{38}$$

where

$$f(\alpha) \equiv \min\left[\frac{1}{2}\sum_{j\neq i}^{N_d} q_i q_j \Gamma(\overline{r_i}, \phi_i, \overline{r_j}, \phi_j) + \sum_{i=1}^{N_d} q_i\left(1 - \frac{q_i}{4\pi}\right)V(\overline{r_i})\right]. \tag{39}$$

Note that in the second term in Eq. (38) the core energy of each defect has been absorbed in the modified core radius a', as defined in Eq. (33). This generates an energy cost for unbinding that can be overcome if $f(\alpha)$ assumes sufficiently large negative values. Hence it is sufficient to study numerically how $\Delta F(\alpha)$ varies as a function of a single parameter, e.g., r_0/a'. As an illustration of this approach, we study explicitly the unbinding of one and two disclination pairs leading to the ground states represented schematically in Fig. 8.

The smooth ground state becomes unstable to the formation of one defect dipole first. The critical aspect ratio above which this scenario occurs can be determined with the aid of Fig. 9, where the function $f(\alpha)$ introduced in Eq. (39) is plotted as a function of the aspect ratio. From Eq. (38) we see that α_{c1} is determined by

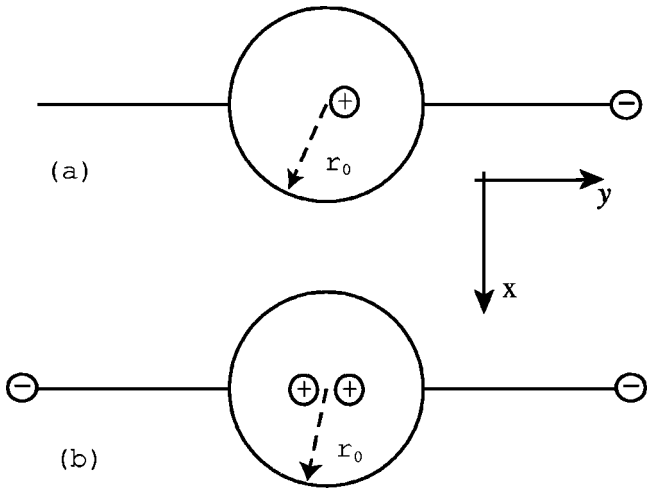

FIG. 8. The equilibrium defects positions are illustrated schematically in the case of one (a) and two (b) dipoles. We assume free boundary conditions at infinity, as in Fig. 3, so that the effect of image charges can be neglected.

$$f(\alpha_{c_1}) = -\frac{q^2}{2\pi}\ln\left(\frac{r_0}{a'}\right). \tag{40}$$

For $r_0/a' = 10^4$ and $q = 2\pi/6$, we obtain a critical aspect ratio $\alpha_{c_1} \approx 3.2$. As a comparison, the approximate condition derived in Eq. (32) gives $\alpha_{c_1} \approx 3$ when used in conjunction with Fig. 6. The rougher estimate in Eq. (34) leads (for $q = 2\pi/6$) to $\alpha_{c_1} \approx 2.6$. This discrepancy is easily understood considering that Eq. (34) was derived by means of a low-α expansion.

The critical aspect ratio α_{c_1} is too low for the two-dipole defect configuration to become energetically favorable with respect to the smooth ground state. Indeed, inspection of Fig. 10 reveals that the critical aspect ratio α_{c_2} for which the

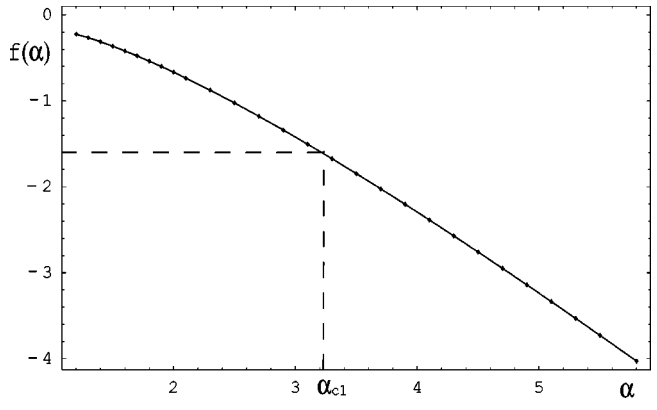

FIG. 9. Plot of $f(\alpha)$ versus the aspect ratio α obtained by minimizing over the single-dipole defect configuration represented schematically in Fig. 8(a). As discussed in the text, the first unbinding transition occurs when $f(\alpha_{c_1})$ is equal to $-q^2/2\pi\ln(r_0/a')$. The value α_{c1} is indicated by the dashed line for $r_0/a' = 10^4$ and $q = 2\pi/6$. Note that no minimum (corresponding to an unbound pair) exists for α less than 1 (approximately); hence the curve cannot be continued to the origin (see Fig. 7).

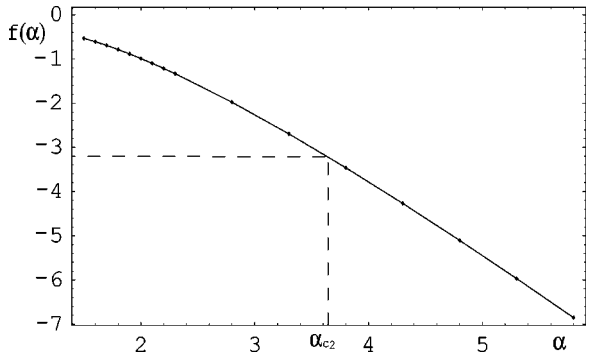

FIG. 10. Plot of $f(\alpha)$ versus the aspect ratio α obtained by minimizing the two-dipole defect configuration represented schematically in Fig. 8(b). The second unbinding transition occurs when $f(\alpha_{c_2})$ is equal to $-(q^2/\pi)\ln(r_0a')$. The value α_{c_2} is indicated by the dashed line for $r_0/a' = 10^4$ and $q = 2\pi/6$ (compare with Fig. 9).

"two-dipole instability" sets in is approximately equal to 3.6 for the same choice of parameters used in the single-pair case. Note that, in the presence of two dipoles, the energy cost arising from the second term in Eq. (38) is twice as large because there are four defects rather than two. However, for $\alpha \gtrsim 4.2$, generating two dipoles becomes more energetically favored than a single dipole (see Fig. 11). The approach illustrated here can be used to calculate a cascade of defect-unbinding instabilities at critical aspect ratios α_{c_i} involving higher number of dipoles and their equilibrium configurations in the ground state. Note that the unbinding eventually stops since the integrated Gaussian curvature in the top cup cannot exceed 2π. We expect the qualitative features of our analysis to be independent of the exact shape of the bumpy substrate although the specific values α_{c_i} depend on the geometry and the choice of the microscopic parameters a and E_c. Finally, we emphasize that the curvature-induced unbinding is similar to a first order transition and occurs for rather pronounced deviations from flatness (i.e., large α).

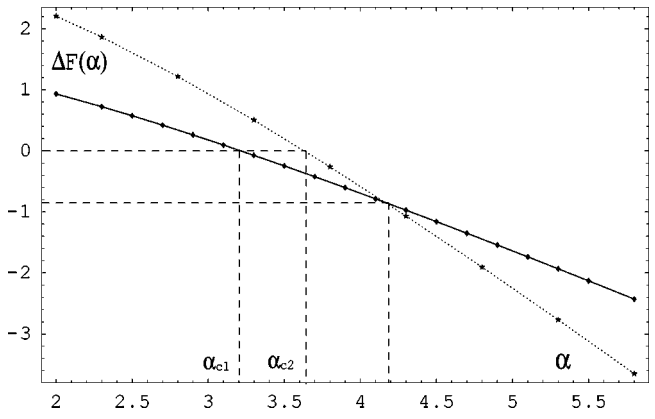

FIG. 11. Plot of $\Delta F(\alpha)/K_A$ versus α corresponding to a single dipole (continuous line) and two dipoles (dotted line) for $r_0/a' = 10^4$. The critical aspect ratios α_{c_1} and α_{c_2} are indicated by dashed lines. Note that the aspect ratio for which the two-dipole configuration becomes energetically favored occurs for $\alpha > 4.2$.

C. Single vortex instability

The unbinding of defect pairs may not be the most likely scenario if the size of the system R is sufficiently small. In this case, the creation of a single vortex at the center of the bump may become energetically favorable for lower aspect ratios than required by the defect dipole instability. The equation for the bond-angle field $\theta_s(\mathbf{u})$ for a single defect of charge q at the center of the bump is given by

$$\theta_s(\phi) = \left(\frac{q}{2\pi} - 1\right)\phi, \tag{41}$$

where the bond angle is measured with respect to the rotating basis vectors corresponding to the polar coordinates discussed in Sec. II B. Upon substituting $\theta_s(\phi)$ in Eq. (2) and subtracting the free energy $\mathcal{F}_0$ corresponding to the defect-free texture we obtain

$$\frac{\Delta F(\alpha)}{K_A} = \frac{q^2}{4\pi}\ln\left(\frac{\Re(R)}{a}\right) + q\left(1 - \frac{q}{4\pi}\right)V(0) + q^2\frac{E_c}{K_A}, \tag{42}$$

where E_c was added by hand. The same result is obtained by using the more general formalism developed in Appendix D. Indeed, by letting the position of an isolated defect tend to the center of the bump in Eq. (D24) we obtain the energy of the singular field in the case of free boundary conditions and the result matches Eq. (42). As discussed in Appendix D, a defect located at r_i is attracted to the boundary at R for free boundary conditions. One can think of this interaction as resulting from an image defect of opposite sign behind the edge of the sample at position r_i' such that the following relation holds in terms of the conformal radius $\Re(r')$:

$$\Re(r_i') = \frac{\Re(R)^2}{\Re(r_i)}. \tag{43}$$

This result can be understood by analogy to the familiar electrostatic problem of a charged line located a distance r_i from the center of a cylindrical grounded conductor whose axis is parallel to it [35]. The analogy becomes precise if one lets $r_i \to \Re(r_i)$ as explained in Appendix D.

If the geometric potential is not strong enough (as in the flat space limit $\alpha=0$), the defect will migrate to the edge of the sample and annihilate with its image leaving a smooth field. On the other hand, when the aspect ratio is sufficiently large, the defect can lower its energy by sitting at the center of the bump. Comparison of Eq. (42) with Eq. (31) shows that, unless $R \gg r_0$, the energy of the single vortex instability will be lower than or at least comparable to the unbinding of a defect dipole. In fact, the threshold α_s that α needs to exceed to trigger the single defect instability is easily obtained if the values of the geometric potential at the origin are tabulated for different aspect ratios, as illustrated in Fig. 5. The condition for single vortex generation reads

$$|V(0)| > \frac{q}{(q-4\pi)}\ln\left(\frac{R}{a'}\right). \tag{44}$$

Using the same method adopted to derive Eq. (34) we obtain an estimate of how α_s depends on R/a' [compare with Eq. (34)]:

$$\alpha_s^2 \approx \frac{4q}{(4\pi - q)}\ln\left(\frac{R}{a'}\right). \tag{45}$$

The single vortex instability is reminiscent of vortex generation in rotating superfluid helium with α playing the role of the angular speed Ω. For a volume of helium contained in a cylindrical vessel of radius R and rotating uniformly with constant angular speed, the critical value Ω_{c_1} above which defect generation occurs is given by [36]

$$\Omega_{c_1} \approx \frac{K}{2\pi R^2}\ln\left(\frac{R}{a}\right), \tag{46}$$

where $K = 2\pi\hbar/m_{He}$ is the magnitude of the quantum of circulation and a the core radius.[2] Note that Ω_{c_1} decreases as R increases, unlike α_s which diverges logarithmically. Thus, the single defect instability studied here is a finite size effect. In contrast, the disclination unbinding studied earlier in this section does not depend on the system size because of charge neutrality. Hence the thermodynamic limit can be safely taken, provided the characteristic length over which the curvature varies (i.e., r_0) is not too large compared to a [see Eq. (34)].

In considering the case of small system size, it is important to keep in mind two assumptions implicit in the present treatment. The radius of curvature r_0/α must be much larger than the core radius everywhere for the continuum approach to be valid, that is, $r_0 \gg \alpha a$. Additionally, the Gaussian curvature must be vanishingly small at the edge of the system which requires R to be larger than a few r_0.

D. Lattice of bumps, valleys, and saddle points

In some experimental realizations perhaps modeled on those of Ref. [12] the topography will be periodic. In this section we discuss qualitatively how the results described above generalize to a two-dimensional lattice of bumps with variable aspect ratio for both square and triangular lattices. A more quantitative approach to this problem would involve finding conformal set of coordinates for periodic boundary conditions. This is possible in principle but more involved since cylindrical symmetry is now lost. Nonetheless, the intuition gained by studying the single bump allows us to make some guesses for the ground state. We first note that the geometric potential generated by the lattice of bumps is not simply the superposition of results for single bump potentials. This is caused by the nonlinear relation between the surface height and the Gaussian curvature acting as a source for the geometric potential. To explore this point further, consider what happens when four bumps are placed at the

[2] A similar mechanism applies to superconductors in a uniform magnetic field.

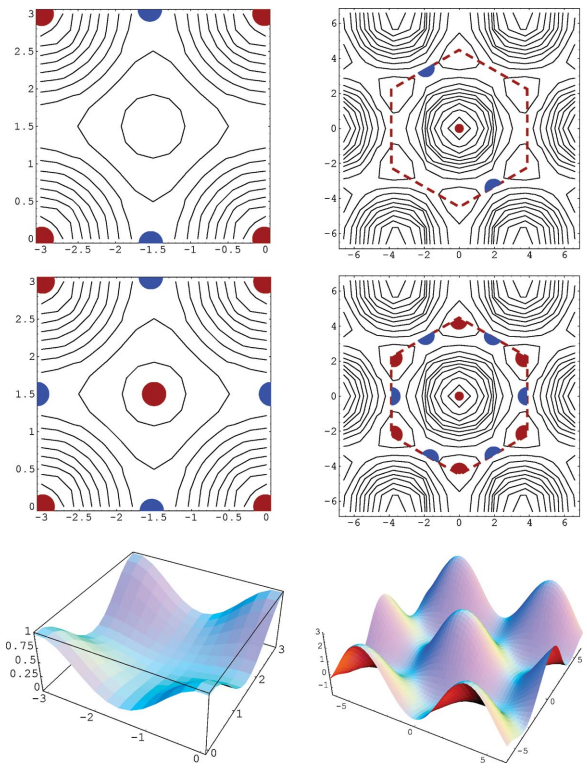

FIG. 12. (Color online) (Top) Ground states for square (left) and triangular (right) arrays of bumps. The first and second rows correspond to moderate values of the aspect ratio α, respectively. For simplicity, we assume that r_0, the bump width, is comparable to the lattice spacing. Positive defects (red dots) "screen" regions of positive Gaussian curvature while negative ones (blue dots) are located on the saddles of the "hilly" landscape.

vertices of a square. At the center of the square a minimum of the height function occurs corresponding to a *new* region of positive Gaussian curvature. This effect is particularly acute for $r_0 \leqslant L$, where L is the bump spacing. In general interference between bumps creates a dual lattice of valleys. A similar breakdown of the superposition principle arises for triangular lattices.

As the aspect ratio of hilly landscapes such as those shown in Fig. 12 is increased, defects can be created to screen the Gaussian curvature. Their positions can be guessed by considering a unit cell of the lattice such that the integrated Gaussian curvature vanishes. For a square lattice, we conjecture that the first topography induced transition is associated with the appearance of positive defects at the top of the bumps and negative ones halfway between them in the vertical or horizontal direction (see Fig. 12). This twofold degeneracy is compatible with the symmetry of the lattice and analogous to the freedom in choosing the axis along which the first disclination dipole appears on the single bump. The negative defects are shared between two adjacent cells while the positive ones are shared among four cells thus ensuring overall charge neutrality. As the value of α increases even more, one might expect an additional positive defect appears in the valley located at the center of each cell and two additional negative defects shared with the adjacent cells are created between the bumps at right angles to the direction discussed above (see Fig. 12).

For the triangular lattice, we conjecture that the first transition corresponds to positive defects on top of the bumps and negative ones between the bumps along one of the three axis of symmetry of the unit cell. As the value of the aspect ratio is increased, additional positive defects appear on the six minima of the surface and negative ones are generated along the remaining two axes of symmetry of the unit cell (see Fig. 12). A simple count of the total defect charges enclosed in the unit cell shows that this scenario also satisfies the requirement of defect charge neutrality.

IV. DEFECT DECONFINEMENT

With potential experiments in mind [23], it is interesting to consider the case of hexatic order on a bump encircled by a circular wall of radius $R \gg r_0$ which aligns the hexatic bond angles. As a simple model, imagine an array of hexagons which locally achieve a common orientation tangential to the wall [see Fig. 18(b) below]. The hexatic order parameter will thus rotate by 2π upon making a circuit of the wall, insuring that at least six defects of "charge" $2\pi/6$ must be included in the ground state for all values of the aspect ratio. These boundary-condition-induced defects will interact with the Gaussian curvature of the bump and with the wall. The N_d defects contribute large (constant) self-energies of the form $\Sigma_{i=1}^{N_d} K_A q_i^2 \ln(R/a)$ that dominate the total energy for sufficiently large systems. Since $\Sigma_{i=1}^{N_d} q_i$ must be equal to 2π, the energy is minimized when the defects split up into the smallest possible charges.

The equilibrium defect configuration must minimize the free energy taking into account the confining potential generated by the Gaussian curvature and the interactions of the defects with the boundary and among themselves. The repulsive force exercised by the wall on a defect located at $\Re(r_i)$ in the conformal plane can be computed by placing an image defect of same charge outside the wall at position $\Re(R)^2/\Re(r_i)$. The mathematics resembles the problem of finding the magnetic field of a line current located at a given distance r_i from the center of a cylinder of high-permeability material and whose radius R is greater than r_i [35]. The analogy is complete upon performing the change of coordinates $r \to \Re(r)$ and identifying the gradient of the bond angle $\partial_\alpha \theta(\mathbf{u})$ with the magnetic field. This is explained in detail in Appendixes C and D where we introduce a conjugate function $\chi(\mathbf{u})$ analogous to the vector potential that simplifies the analysis of this problem. Thus, each of the N_d defects will also interact with an equal number of image defects. This situation can be described mathematically by deriving an appropriate Green's function Γ^N that includes the images, as discussed in Appendix D [see Eq. (D19)]. The resulting free energy F^N reads

$$\frac{F^N}{K_A} = \frac{1}{2}\sum_{j\neq i}^{N_d} q_i q_j \Gamma^N(x_i;x_j) + F_0 + \sum_{i=1}^{N_d} q_i \left(1 - \frac{q_i}{4\pi}\right) V(r_i) + \sum_{i=1}^{N_d} \frac{q_i^2}{4\pi} \ln\left(\frac{\Re(R)}{a}\right) - \sum_{i=1}^{N_d} \frac{q_i^2}{4\pi} \ln\left(1 - x_i^2\right), \tag{47}$$

where F_0 is defined in Eq. (17) and the Green's function $\Gamma^N(x_i;x_j)$ is given by

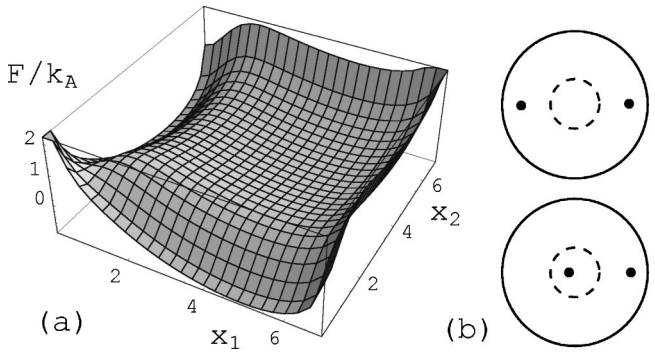

FIG. 13. (a) The free energy for a nematic (double headed vector field) living on a Gaussian bump surrounded by an aligning circular wall is plotted for $\alpha=2$ as a function of the scaled radial coordinates x_1 and x_2 of the two disclinations. The radial coordinates have been scaled by r_0 and the size of the system is $R=7r_0$. Note that the energy plot is symmetric with respect to the line $x_1=x_2$. (b) Schematic illustration of the positions of the two disclinations (black dots) corresponding to the deep energy minima at positions $x_1=0.04$ and $x_2=4.9$ (or vice versa) and to a shallow minimum at $x_1=x_2=4.7$. The two defects are on opposite sides of the bump. The continuous line corresponds to the circular boundary and the dashed one to the circle of zero Gaussian curvature and radius r_0 (drawing not to scale).

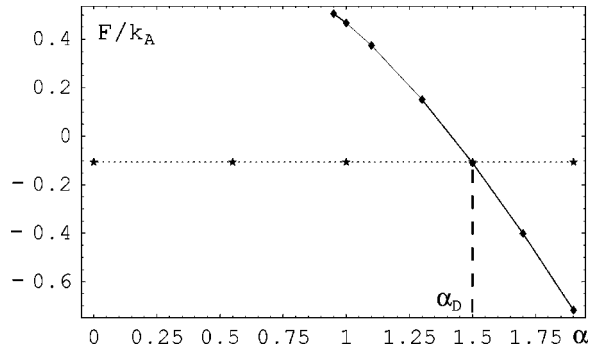

FIG. 14. Plot of the free energy of a nematic (double headed vector field) on a Gaussian bump encircled by an aligning wall as a function of α. The dotted line represents the energy of the fully deconfined configuration in Fig. 13(b) top panel while the continuous line corresponds to the defect pattern illustrated in the bottom panel of Fig. 13(b). The energy of the fully deconfined configuration is approximately independent of α because the two disclinations are far away from the bump.

$$\Gamma^N(x_i;x_j) = -\frac{1}{4\pi}\ln[x_i^2+x_j^2-2x_ix_j\cos(\phi_i-\phi_j)] - \frac{1}{4\pi}\ln[x_i^2x_j^2+1-2x_ix_j\cos(\phi_i-\phi_j)]. \quad (48)$$

The last term accounts for the interaction with the image defects and the superscript N indicates Neumann boundary conditions on an appropriate potential function. Here, we use scaled coordinates in the conformal plane $x_i \equiv \Re(r_i)/\Re(R)$. The interaction of the defects with the curvature is not affected by the presence of the distant wall.

To provide an illustration of the combined effect of curvature and boundary conditions on tangential vector order, we first consider the simpler case of a nematic order parameter with periodicity equal to π. This simplified model neglects differences in the elastic constants for bend and splay and does not incorporate any effect due to the uniaxial coupling of the nematogens to the curvature. In this case, minimization of the logarithmically diverging part of the free energy [fourth term in Eq. (47)] suggests that there will be only two disclinations of charge $q=\pi$ displaced along a radial direction [see Fig. 13(b)]. By applying Eq. (47), we can parametrize the energy of the system in terms of the scaled radial coordinates x_1 and x_2 of the two disclinations. The resulting energy landscape is plotted in Fig. 13 (for $\alpha=2$ and $R=7r_0$) and clearly reveals two minimal-energy configurations. The first minimum corresponds to one disclination confined at the top of the bump (slightly shifted from the center) and the other at a radial distance approximately 70% of R [see Fig. 13(b) bottom panel]. The second minimum corresponds to a fully deconfined state with both disclinations placed symmetrically at approximately 67% of R (see Fig. 13(b) top panel). As the aspect ratio is raised even further, the saddle in the energy landscape of Fig. 13(a) becomes a minimum corresponding to a configuration in which both disclinations are confined in the cup of positive Gaussian curvature by the geometric potential.

As illustrated in Fig. 14, there is a critical value of the aspect ratio, $\alpha_D \simeq 1.5$, above which it is energetically favorable for the system to have one disclination confined at the top of the bump. For $\alpha < \alpha_D$ the fully deconfined configuration becomes energetically favorable, but the two minima can still coexist. As α is decreased even further, the repulsion between the two disclinations overcomes the confining force of the geometric potential and makes the second minimum in Fig. 13(a) (corresponding to the partially confined configuration) disappear altogether. This "spinodal point" occurs for $\alpha \approx 0.9$ on the Gaussian bump. The specific values of the critical aspect ratios are geometry dependent, but the generic mechanism of deconfinement depends only on a large separation of the length scales r_0 and R that control the interaction with the curvature and the boundary respectively.

The analysis for the hexatic case is complicated by the fact that more defect configurations are possible when six defects are present. We start by noting that even in flat space ($\alpha=0$) there are two natural low-energy defect configurations with high symmetry: the ground state corresponding to the six defects sitting at the vertices of a hexagon and a higher-energy state given by a pentagonal distribution of defects with the sixth defect sitting at the center of the circular sample [see Fig. 15(b)]. As the aspect ratio is raised, the pentagonal arrangement becomes energetically favored since it pays to have a defect confined in the (geometric) potential well at the origin [see Fig. 15(a)]. To study the transition, it is useful to derive expressions for the energy of the two defect configurations as a function of the radius of the outer defect ring r. Every defect (except the one at the origin, possibly) has the same scaled coordinate $x_i=x$ and the angles between two defects are integer multiples of $2\pi/n$ where n is the number of defects in the outer ring ($n=5$ for the pentagon and $n=6$ for the hexagon). In this case, the sums involved in

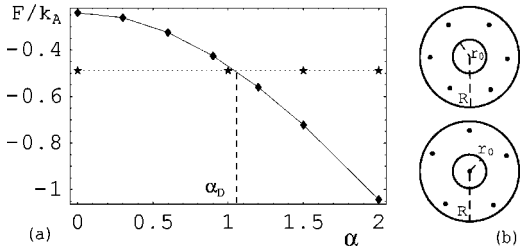

FIG. 15. Plot of the free energy of a hexatic phase (draped on the Gaussian bump encircled by a wall) as a function of α. The dotted line represents the energy of the hexagonal configuration illustrated in the top panel on the left while the continuous line corresponds to the pentagonal arrangement in the bottom panel. The outer defect rings in both configurations are approximately 90% of R. The critical aspect ratio α_D corresponding to the deconfinement transition discussed in the text is indicated by the dashed line.

the first (interaction) term in Eq. (47) can be efficiently evaluated using the following identity:

$$\frac{1}{2}\sum_{i}^{n-1} \ln\left[p^2+1-2p\cos\left(\frac{2\pi i}{n}\right)\right] = \ln(1-p^n) - \ln(1-p). \tag{49}$$

Upon using Eq. (49) with $p=1$ and $p=x^2$ to evaluate the sums arising from the first and the second terms of the Green's function in Eq. (48), respectively, we obtain the free energy F_H for the hexagonal configuration:

$$\frac{F_H(\alpha)}{K_A} = -\frac{\pi}{6}\ln\left[\left(\frac{\Re(r)}{\Re(R)}\right)^5 - \left(\frac{\Re(r)}{\Re(R)}\right)^{17}\right] - \frac{\pi}{6}\ln 6 + \frac{11\pi}{6}V(r) + \frac{\pi}{6}\ln\left[\frac{\Re(R)}{a}\right]. \tag{50}$$

The free energy for the pentagonal configuration F_P is readily obtained after similar manipulations:

$$\frac{F_P(\alpha)}{K_A} = -\frac{5\pi}{36}\ln\left[\left(\frac{\Re(r)}{\Re(R)}\right)^6 - \left(\frac{\Re(r)}{\Re(R)}\right)^{16}\right] - \frac{\pi}{2}\ln 2 + \frac{11\pi}{36}V(0) + \frac{55\pi}{36}V(r) + \frac{\pi}{6}\ln\left[\frac{\Re(R)}{a}\right]. \tag{51}$$

Note that these manipulations are very similar to the ones necessary to describe superfluid helium in a cylinder of radius R [37]. In fact, the superfluid problem is analogous to the case of hexatic order with *free* boundary conditions on a circular boundary of radius R (see Appendix D). The rather unusual form of the argument of the logarithm in Eqs. (50) and (51) arises from the sum over the image defects whose positions depend nonlinearly on the position of the defects themselves.

Minimization of Eqs. (50) and (51) with respect to r fixes the distance of the outer defects. The resulting minimal energies F_P and F_H are plotted as functions of α in Fig. 15(a).

For the critical value α_D, $F_P < F_H$ can be easily estimated by realizing that F_H is approximately independent of α because the disclinations are far from the bump. On the other end, F_P decreases with increasing α because the confined disclination is trapped in a potential well whose depth is approximately given by $-\frac{11}{144}\pi\alpha^2$ [see the second term of Eq. (51) and the low α expansion for $V(0)$ derived in Eq. (26)]. The critical aspect ratio α_D for which the deconfinement transition occurs can be estimated by setting the depth of this potential well equal to the energy difference between the hexagon and pentagon configurations in flat space. The latter can be read off from the energy diagram in Fig. 15(a) and the result is approximately $0.3K_A$ which leads to $\alpha_D \sim 1.1$ in agreement with the value indicated in Fig. 15(a).

As the aspect ratio is raised even further, less symmetric defect configurations become energetically favored corresponding to a larger number of disclinations confined in the cup of positive Gaussian curvature. For example, when two disclinations are confined within $r=r_0$, the outer defect ring is given by four defects approximately located at the vertices of a square. We note that these defect configurations cease to exist at low aspect ratios because they require the geometric potential to overcome the strong repulsive interaction between the confined defects. As discussed earlier for Fig. 14, the actual values of the aspect ratios involved depend on the specific geometry of the substrate. However, the basic mechanism behind the deconfinement transition is more general.

Note that, as α increases, the geometric mechanism of defect-dipole unbinding discussed in the last section may also set in. Because of the presence of one or more positive defects at the top of the bump, the critical aspect ratio necessary to unbind one dipole will be larger than what was calculated before. If dipole unbinding does occur, the new defects will "decorate" the existing patterns by adding new positively charged disclinations in the region of positive Gaussian curvature and expelling the negative ones in the external region of the bump ($r > r_0$) where the Gaussian curvature is also negative (see Fig. 1).

V. CONCLUSION

We have discussed how the varying curvature of a surface such as a "Gaussian bump" can trigger the generation of single defects or the unbinding of dipoles, even if no topological constraints or entropic arguments require their presence. This mechanism is independent of temperature if the system is kept well below its Kosterlitz-Thouless transition temperature. It would be interesting to revisit Kosterlitz-Thouless defect-unbinding transitions on surfaces of varying Gaussian curvature in the presence of a quenched topography [13] in the light of the present work. One might also explore the *dynamics* of the delocalization transition that occurs when a bump is confined by a circular edge and the aspect ratio is lowered until the defects, initially confined on top of the bump by the geometric potential, are forced to "slide" toward the boundary. Quantitative studies of periodic arrangements of bumps would be interesting and could be inspired by fruitful analogies with methods and ideas from solid state physics.

We also hope to extend this work by considering crystalline order on bumpy topographies and taking explicitly into account the screening of clouds of dislocations and possible

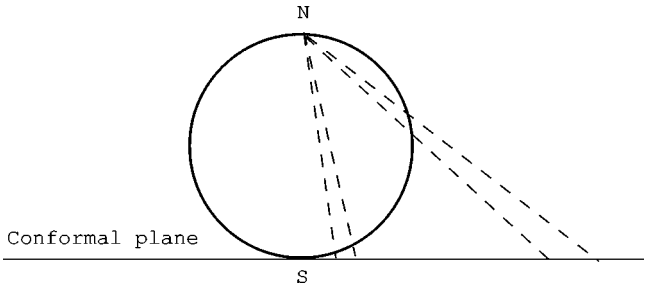

FIG. 16. Graphic construction of the stereographic projection. Regions close to the north pole have larger images in the conformal plane than regions of equal areas close to the south pole. The stereographic projection preserves the topology of the surface provided all points at infinity are identified with the north pole.

generation of grain boundaries [16]. Such an analysis would facilitate comparison with experiments performed with a single grain of block copolymer spherical domains[3] on a suitably patterned substrate [12,23].

ACKNOWLEDGMENTS

We wish to acknowledge helpful conversations with M. Bowick, B. I. Halperin, A. Hexemer, E. Kramer, S. Minwalla, K. Papadodimas, A. Travesset, and A. Turner. This work was supported by the National Science Foundation, primarily through the Harvard Materials Research Science and Engineering Laboratory via Grant No. DMR-0213805 and through Grant No. DMR-0231631.

APPENDIX A: GREEN'S FUNCTION AND ISOTHERMAL COORDINATES

The analysis of ordered phases on curved substrates can be simplified by rewriting the original metric of the surface $g_{ab}(\mathbf{u})$ in terms of a convenient set of coordinates $\mathbf{x}(\mathbf{u}) = (x(\mathbf{u}), y(\mathbf{u}))$ such that the new metric $\tilde{g}_{ab}(\mathbf{x})$ reads

$$\tilde{g}_{ab}(\mathbf{x}) = e^{\rho(x,y)}\delta_{ab}. \tag{A1}$$

The metric $\tilde{g}_{ab}$ differs from the flat space one δ_{ab} only by a conformal factor $e^{\rho(x,y)}$ that embodies information on the curvature of the surface [31]. These *isothermal coordinates* can be used to map arbitrary corrugated surfaces onto the plane [38]. The mapping is conformal so angles are left unchanged but areas are stretched according to the position-dependent conformal factor $e^{\rho(x,y)}$. A familiar example is provided by the stereographic projection that maps a sphere onto the conformal plane as illustrated in Fig. 16.

The Green's function assumes a very simple form after a conformal transformation, because the Laplace operator reduces to the familiar flat space result when expressed in terms of isothermal coordinates. In what follows, we demonstrate that this transformation provides the basis for an efficient strategy to determine the Green's function on a bumpy substrate. We start by deriving the radial change of coordinates $\Re(r)$ that transforms the original metric of the Gaussian bump, i.e.,

$$ds^2 = \left(1 + \frac{\alpha^2 r^2}{r_0^2} e^{-r^2/r_0^2}\right) dr^2 + r^2 d\phi^2, \tag{A2}$$

into the locally flat metric (in polar coordinates),

$$ds^2 = e^{\rho(r)}(d\Re^2 + \Re^2 d\phi^2), \tag{A3}$$

where $\rho(r)$ and $\Re(r)$ are independent of the azimuthal coordinate ϕ because of cylindrical symmetry. This metric is equivalent to $\tilde{g}_{ab}(\mathbf{x})$ upon switching from Cartesian (x,y) to polar coordinates $(\Re(r), \phi)$. To simplify the notation we introduce the α-dependent function $l(r)$ defined by

$$l(r) \equiv 1 + \frac{\alpha^2 r^2}{r_0^2} \exp\left(-\frac{r^2}{r_0^2}\right), \tag{A4}$$

and plotted in Fig. 2 for different choices of α.

The equivalence of the metrics in Eq. (A2) and (A3) requires that $\Re(r)$ satisfy the differential equation

$$\frac{d\Re}{\Re} = \frac{\sqrt{l(r)}}{r} dr. \tag{A5}$$

The conformal factor is thus given by

$$e^{\rho(r)} = \left(\frac{r}{\Re}\right)^2. \tag{A6}$$

The solution of Eq. (A5) is

$$\Re(r) = Ar \exp\left(-\int_r^c \frac{dr'}{r'}[\sqrt{l(r')} - 1]\right), \tag{A7}$$

where it is convenient to set the arbitrary constants A and c to unity and infinity, respectively. This nonlinear stretch of the radial coordinate leaves the origin and the point at infinity invariant and can be concisely written as

$$\Re(r) = re^{V(r)}, \tag{A8}$$

where the function $V(r)$ defined by

$$V(r) \equiv -\int_r^\infty dr' \frac{\sqrt{l(r')} - 1}{r'}, \tag{A9}$$

plays an important role in our formalism and its interpretation as a sort of geometric potential is explored in detail in Appendix B.

The Poisson equation for the Green's function $\Gamma(\mathbf{u},\mathbf{u}')$ on a surface with metric tensor $g_{\alpha\beta}$ and point source $\delta(\mathbf{u},\mathbf{u}')$ reads [26]

$$D^\alpha D_\alpha \Gamma(\mathbf{u},\mathbf{u}') = -\frac{\delta(\mathbf{u},\mathbf{u}')}{\sqrt{g}}, \tag{A10}$$

where the covariant Laplacian is given for general coordinates by

[3]The radius of block-copolymer spherical cores is of the order of a few nanometers and their spacing tens of nanometers. These values can be tuned by suitably choosing the block copolymers and varying their volume fraction.

$$D^{\alpha}D_{\alpha} \equiv (1/\sqrt{g})\partial_{\alpha}[\sqrt{g}g^{\alpha\beta}\partial_{\beta}]. \tag{A11}$$

The conformal change of coordinates transforms $\sqrt{g(r,\phi)}$ into $e^{\rho(r)}\sqrt{g(\Re,\phi)}$ and $g^{\alpha\beta}(r,\phi)$ into $e^{-\rho(r)}g^{\alpha\beta}(\Re,\phi)$. The factors of $e^{\rho(r)}$ inside the square brackets in Eq. (A11) then cancel and we are left with the flat space Laplacian in the polar coordinates $(\Re(r),\phi)$. We conclude that $\Gamma(\mathbf{u},\mathbf{u}')$ is simply the Green's function of an undeformed plane expressed in terms of the polar coordinates $(\Re(r),\phi)$:

$$\Gamma(\mathbf{u},\mathbf{u}') = -\frac{1}{4\pi}\ln[\Re(r)^2 + \Re(r')^2 - 2\Re(r)\Re(r') \times\cos(\phi-\phi')], \tag{A12}$$

where an arbitrary additive constant C (which can be used to satisfy boundary conditions at infinity) has been dropped. We note that $\Gamma(\mathbf{u},\mathbf{u}')$ differs from the flat space Green's function by a nonlinear stretch of the radial coordinate. In Appendix C, we will use $\Gamma(\mathbf{u},\mathbf{u}')$ to solve Poisson's equation on an infinite bumpy domain and calculate the energy stored in the field. As in flat space, the Green's function $\Gamma(\mathbf{u},\mathbf{u}')$ will be suitably modified in a finite system in a way that depends on the boundary conditions chosen at the edge of the sample (see Appendix D).

We conclude this appendix by evaluating $\Gamma(\mathbf{u},\mathbf{u}')$ when the two points $\mathbf{u}$ and $\mathbf{u}'$ are assumed to be separated by a fixed distance a small enough so that the surface can be approximated by the local tangent plane to the Gaussian bump. This short distance behavior will be useful when evaluating the effect of a *constant* core radius on the energetics of a disclination at an arbitrary position. The fixed microscopic length a on the bump is stretched when projected in the conformal plane (see, e.g., Fig. 16) and assumes the position-dependent value $\lambda(x,y)$ given by

$$\lambda(x,y) = ae^{-\rho(x,y)/2}. \tag{A13}$$

For a Gaussian bump cylindrical symmetry requires that $\lambda(r,\phi)$ is dependent only on r and can be explicitly written upon using Eqs. (A6) and (A8) as

$$\lambda(r,\phi) = a\frac{\Re(r)}{r} = ae^{V(r)}. \tag{A14}$$

We can now evaluate $\Gamma(\mathbf{u},\mathbf{u}')$ in the limit $\mathbf{u}'\to\mathbf{u}+\mathbf{a}$, where this concise notation means that the two points on the surface with coordinates $\mathbf{u}$ and $\mathbf{u}'$ are separated by an infinitesimal distance a measured on the bump. It does not matter in what direction the two points approach each other as long as a is small compared to the local radii of curvature. Upon using Eqs. (A12) and (A14), we obtain

$$\Gamma(\mathbf{u},\mathbf{u}+\mathbf{a}) = -\frac{1}{4\pi}\ln(a^2) - \frac{V(r)}{2\pi}. \tag{A15}$$

We note that $\Gamma(\mathbf{u},\mathbf{u}+\mathbf{a})$ for fixed a is not a constant as in flat space but varies with position as the function $V(r)$, reflecting the lack of translational invariance on an inhomogeneous surface, where properties such as the Gaussian curvature also vary with position.

APPENDIX B: GEOMETRIC POTENTIAL

In this appendix we present two equivalent ways of determining the explicit form of the geometrical potential $V(\mathbf{u})$ valid for azimuthally symmetric surfaces like the Gaussian bump. The starting point is the general definition introduced in Sec. II C:

$$V(\mathbf{u}) \equiv -\int dA' G(\mathbf{u}')\Gamma(\mathbf{u},\mathbf{u}'), \tag{B1}$$

with the Green's function Γ as defined in Eq. (A10). In the electrostatic analogy, $V(\mathbf{u})$ is thus the potential induced by a continuous distribution of "charge" represented by the Gaussian curvature (with sign reversed). We shall derive an analogue of the Gauss law for corrugated surfaces where the curvature of the surface (with sign reversed) plays the role of a continuous density of electrostatic charge.

The first derivation makes use of the fact that $V(\mathbf{u})$ is a scalar under conformal transformations. This symmetry can be checked explicitly by applying the same reasoning adopted for the equation satisfied by the Green's function in Appendix A to Eq. (B1). In fact, upon operating on both sides of Eq. (B1) with the covariant Laplacian and using Eq. (A10), the defining equation for the geometric potential can be cast into the differential form

$$D^{\alpha}D_{\alpha}V(\mathbf{u}) = G(\mathbf{u}). \tag{B2}$$

The Gaussian curvature in Eq. (B2) can be written in conformal coordinates [31] as

$$G(x,y) = -e^{-\rho(x,y)}(\partial_x^2+\partial_y^2)\frac{\rho(x,y)}{2}, \tag{B3}$$

where $\rho(x,y)$ is the conformal factor introduced in Appendix A. Similarly the left hand side of Eq. (B2) can be expressed in conformal coordinates [31] as

$$D^{\alpha}D_{\alpha}V(\mathbf{x}) = +e^{-\rho(x,y)}(\partial_x^2+\partial_y^2)V(x,y). \tag{B4}$$

Upon substituting Eqs. (B3) and (B4) in Eq. (B2), we conclude immediately that the geometric potential in conformal coordinates $V(\mathbf{x})$ is given by

$$V(x,y) = -\frac{\rho(x,y)}{2}. \tag{B5}$$

Upon using Eqs. (A6), (A8), and (A9), to substitute in Eq. (B5), one obtains the explicit form of the geometric potential for the bump parametrized by the coordinates (r,ϕ):

$$V(r) = -\int_r^{\infty} dr'\frac{\sqrt{l(r')}-1}{r'}, \tag{B6}$$

where the α-dependent function $l(r)$ was defined in Eq. (A4) and plotted in Fig. 2. The result of the integration in Eq. (B6) is independent of ϕ because of azimuthal symmetry. The upper limit of integration is chosen consistently with Eq. (B2) as usually done in electrostatics.

A second derivation of this result is obtained by making explicit use of the azimuthal symmetry of the bump and deriving a covariant form of Gauss' law which allows an

intuitive understanding of the interaction between defects and curvature. This curved space version of Gauss' law illuminates the electrostatic analogy used throughout the text. The gradient of the geometric potential defines an "electric field" E_α given by

$$E_\alpha \equiv -D_\alpha V(\mathbf{u}) = \int dA' G(\mathbf{u}') D_\alpha \Gamma(\mathbf{u},\mathbf{u}'), \tag{B7}$$

where we have used Eq. (B1). One might expect that the flux of the vector E^α through a closed loop is proportional to the enclosed Gaussian curvature in analogy with Gauss' law that relates the flux of the electric field to the electrostatic charge enclosed. To prove this assertion, we invoke the generalized Stokes formula [26] that relates the surface integral over A of the gradient of a field to its flux through the contour loop C:

$$\int_A dA\, D_\alpha E^\alpha = -\oint_C du^\alpha \gamma_\alpha{}^\beta E_\beta. \tag{B8}$$

The covariant antisymmetric tensor $\gamma_{\alpha\beta}$ is given by

$$\gamma_{\alpha\beta} = \sqrt{g}\,\epsilon_{\alpha\beta}, \tag{B9}$$

where $\epsilon_{\alpha\beta}$ is the antisymmetric tensor with $\epsilon_{r\phi} = -\epsilon_{\phi r} = 1$. Similarly $\gamma^{\alpha\beta}$ equals $\epsilon_{\alpha\beta}/\sqrt{g}$ and the following identity holds [21]:

$$\gamma^{\alpha\sigma}\gamma_{\sigma\beta} = -\delta^\alpha_\beta. \tag{B10}$$

The tensor $\gamma_\alpha{}^\beta = \gamma_{\alpha\sigma} g^{\sigma\beta}$ performs anticlockwise rotations of $\pi/2$ when acting on an arbitrary tangent vector V_β, as can be checked by evaluating $V^\alpha \gamma_\alpha{}^\beta V_\beta = \gamma_{\alpha\beta} V^\alpha V^\beta = 0$, where we have used the antisymmetry of $\gamma_{\alpha\beta}$. Thus, the vector $du^\alpha \gamma_\alpha{}^\beta$ in Eq. (B8) represents an infinitesimal contour length times the inward unit vector perpendicular to it. The dot product with the field E_β then generates the flux. To calculate the flux piercing a circular circuit centered on a Gaussian bump, we will need to explicitly evaluate $\gamma_\phi{}^r$,

$$\gamma_\phi{}^r = -\frac{r}{\sqrt{l(r)}}. \tag{B11}$$

Upon using Eq. (B7) we can rewrite the left hand side of Eq. (B8) as

$$\int dA\, D_\alpha E^\alpha = \int dA \int dA' G(\mathbf{u}') D_\beta D^\beta \Gamma(\mathbf{u},\mathbf{u}'). \tag{B12}$$

If we now recall the defining Eq. (A10) of the Green's function $\Gamma(\mathbf{u},\mathbf{u}')$ and keep in mind that the Laplacian in Eq. (B12) operates on the variables labeled by $\mathbf{u}'$ (not $\mathbf{u}$), we obtain using Eq. (B8) a general result for the flux piercing a closed loop on the surface, namely,

$$\oint_C du^\alpha \gamma_\alpha{}^\beta E_\beta = \int_A d^2u \sqrt{g} G(\mathbf{u}). \tag{B13}$$

We can explicitely evaluate the right hand side of Eq. (B13) with the aid of Eq. (12). By appealing to the cylindrical symmetry, in the special case of the Gaussian bump one can apply this covariant form of Gauss' theorem to find the radial field $E^r(r)$ in terms of the integrated Gaussian curvature divided by the length of a boundary circle of radius r, with the result

$$E^r = \frac{1-\sqrt{l(r)}}{r l(r)}, \tag{B14}$$

where we used Eqs. (A2) and (B11). The angular component E^ϕ is zero everywhere. Note that $E^r(r)$ vanishes linearly with r for small r and decays like re^{-r^2/r_0^2} for $r \gg r_0$. From Eq. (B14) one can obtain the geometric potential $V(r)$ by performing a line integral,

$$V(r) = \int_r^\infty dr' g_{rr} E^r = -\int_r^\infty dr' \frac{\sqrt{l(r')}-1}{r'}, \tag{B15}$$

which matches the result previously obtained in Eq. (B6).

APPENDIX C: FREE ENERGY ON A CORRUGATED PLANE

In this appendix, we derive the effective free energy for a charge neutral configuration of defects confined on an infinite surface of varying Gaussian curvature with the topology of the plane. A general method was introduced in Ref. [30] that allows treatments of the more complicated case of deformed spheres. A detailed treatment of boundary effects is developed in Appendix D. Here we simply assume that the size of the system is much larger than the size of the bump and that the boundary does not impose any topological constraint to the director of the liquid crystal. The results presented here match those obtained in Appendix D for free boundary conditions, as long as the defects are far from the boundary. Suppose that all the N_d defects have the same circular core radius a which does not depend on where they are located on the surface. This assumption is justified if the radius of curvature r_0/α is much greater than a. In this limit, the microscopic physics that determines a is insensitive to the presence of the curvature and since the bump is locally flat a is approximately constant everywhere. The starting point of our analysis is the free energy expressed in terms of the singular part of the bond angle $\theta_s(\mathbf{u})$,

$$F = \frac{1}{2} K_A \int_S dA\, g^{\alpha\beta} (\partial_\alpha \theta_s - A_\alpha)(\partial_\beta \theta_s - A_\beta). \tag{C1}$$

The cores of the defects are excluded from the area integral in Eq. (C1); hence S is a disconnected domain corresponding to the corrugated surface punctured at the positions $\mathbf{u}_i = (r_i, \phi_i)$ of the defects. In the conformal plane parametrized by the coordinate $\Re(r)$ defined in Eq. (A8), the defect cores are circles whose position-dependent radius is given by $ae^{V(r_i)}$. The boundaries of the "core disks" are labeled by C_i while the circular edge of the sample of radius R is denoted by B (see Fig. 17).

Upon introducing a "Cauchy conjugate" function $\chi(\mathbf{u})$ defined by

$$\partial_\alpha \theta_s - A_\alpha = \gamma_\alpha{}^\beta \partial_\beta \chi, \tag{C2}$$

the free energy in Eq. (C1) can be cast in the form

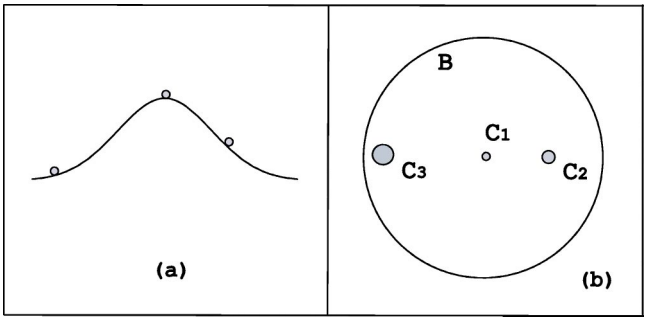

FIG. 17. (a) Defects with fixed core size a on a Gaussian bump encircled by a circular boundary of radius R denoted by B. (b) The size of the vortex cores varies with position when plotted in the conformal plane. One can avoid the singularities associated with the defects cores by puncturing the conformal plane. This introduces circular boundaries C_i of varying radius at the position of each defect in the conformal plane, reflecting corresponding constant core radii on the Gaussian bump.

$$F = \frac{1}{2} K_A \int_S dA\, g^{\alpha\beta} (\partial_\alpha \chi)(\partial_\beta \chi). \tag{C3}$$

In deriving Eq. (C3) we used the identity

$$g^{\mu\nu} \gamma_\mu{}^\alpha \gamma_\nu{}^\beta = g^{\alpha\beta}, \tag{C4}$$

which can be proved with the aid of Eq. (B10) and the discussion following it. Equation (C4) implies that the (covariant) dot product between two vectors after rotating each of them by $\pi/2$ is equivalent to taking the dot product between the two initial vectors. The integral in Eq. (C3) can be rewritten as

$$\frac{F}{K_A} = \frac{1}{2} \int_S dA\, D_\alpha (\chi D^\alpha \chi) - \frac{1}{2} \int_S dA\, \chi D_\alpha D^\alpha \chi, \tag{C5}$$

where

$$D_\alpha (\chi D^\alpha \chi) \equiv (1/\sqrt{g}) \partial_\alpha (\sqrt{g} g^{\alpha\beta} \chi \partial_\beta \chi), \tag{C6}$$

and $D^\alpha D_\alpha$ is defined in Eq. (A11). Upon taking an additional covariant derivative, we can recast Eq. (C2) in the form of a Poisson equation for the electrostaticlike potential $\chi(\mathbf{u})$,

$$D_\alpha D^\alpha \chi(\mathbf{u}) = -\rho(\mathbf{u}), \tag{C7}$$

where the analog of the electrostatic charge density $\rho(\mathbf{u})$ is given by

$$\rho(\mathbf{u}) \equiv \sum_{i=1}^{N_d} q_i \frac{\delta(\mathbf{u}, \mathbf{u}_i)}{\sqrt{g}} - G(\mathbf{u}). \tag{C8}$$

It is useful to compare Eq. (C7) to Eq. (B2) used to define the geometric potential in Appendix B. Both expressions are Poisson equations, the only difference being that the source term of Eq. (C8) includes both the pointlike charges of the defects and the Gaussian curvature with its sign reversed. Hence the Gauss law discussed in Appendix B for the geometric field E_α applies also to $\partial_\alpha \chi$, provided that Eq. (B13) is suitably modified to include the contribution from the topological charges of the defects:

$$\oint_C du^\alpha \gamma_\alpha{}^\beta \partial_\beta \chi = \int_A d^2 \sqrt{g} \left(G(\mathbf{u}) - \sum_{i=1}^{N_d} q_i \frac{\delta(\mathbf{u}, \mathbf{u}_i)}{\sqrt{g}} \right), \tag{C9}$$

where C is the contour enclosing an arbitrary surface A. This relation will be useful later.

We can formally solve for $\chi(\mathbf{u})$ in Eq. (C7) in terms of the Green's function $\Gamma(\mathbf{u}, \mathbf{u}')$ found in Appendix A:

$$\chi(\mathbf{u}) = \int_A dA' \rho(\mathbf{u}') \Gamma(\mathbf{u}, \mathbf{u}'), \tag{C10}$$

where boundary terms have been dropped using charge neutrality and the fact that the edge of the sample is assumed to be far away from the defects. The integral in Eq. (C10) can be evaluated, with the result

$$\chi(\mathbf{u}) = \sum_{i=1}^{N_d} q_i \Gamma(\mathbf{u}, \mathbf{u}_i) - \int_A dA' G(\mathbf{u}') \Gamma(\mathbf{u}, \mathbf{u}'). \tag{C11}$$

Upon using Eq. (B1), we obtain

$$\chi(\mathbf{u}) = \sum_{i=1}^{N_d} q_i \Gamma(\mathbf{u}, \mathbf{u}_i) + V(\mathbf{u}). \tag{C12}$$

We note that the first term is singular at positions $\mathbf{u}_i$ but when χ is substituted in Eq. (C3) the resulting energy is finite because the cores of the defects are excluded from the domain of integration S. Upon substituting Eq. (C7) in the second term of Eq. (C5) we obtain

$$\int_S dA\, \chi D_\alpha D^\alpha \chi = -\int_S dA\, \chi \rho(\mathbf{u}) = \int_S dA\, \chi G(\mathbf{u}), \tag{C13}$$

where we dropped terms involving the δ functions in Eq. (C8) because they vanish everywhere except at the coordinates of the defects which are excluded from the domain of integration S. Upon substituting Eq. (C12) in Eq. (C13) we obtain

$$-\int_S dA\, \chi D_\alpha D^\alpha \chi = \sum_{i=1}^{N_d} q_i V(\mathbf{u}_i) + \int dA \int dA' G(\mathbf{u}) \Gamma(\mathbf{u}, \mathbf{u}') G(\mathbf{u}'), \tag{C14}$$

where we used Eq. (B1).

To evaluate the first term in Eq. (C5), we apply the generalized Stokes formula of Eq. (B8) and convert the surface integrals into line integrals over the boundaries:

$$\int_S dA\, D_\alpha (\chi D^\alpha \chi) = \sum_{i=1}^{N_d} \oint_{C_i} du^\alpha \chi \gamma_\alpha{}^\beta D_\beta \chi - \oint_B du^\alpha \chi \gamma_\alpha{}^\beta D_\beta \chi, \tag{C15}$$

where the difference in sign between the two boundary integrals in Eq. (C15) is due to the fact that the outward normals

for the paths C_i are oriented opposite to the normal for B, the outermost boundary of the system.

To evaluate the last term in Eq. (C15), we note that the flux through the distant boundary B due to a charge neutral distribution of defects is approximately zero, provided that the integrated Gaussian curvature enclosed by the boundary is vanishingly small [see Eq. (C9)]. Hence

$$\chi \oint_B du^\alpha \gamma_\alpha{}^\beta D_\beta \chi \simeq 0, \tag{C16}$$

where we used the fact that χ, defined in Eq. (C2), is approximately constant on B since $\partial_\alpha \theta - A_\alpha \simeq 0$. By contrast, the flux of $\partial_r \chi$ piercing the boundary C_i in Eq. (C15) is approximately equal to the charge q_i of the enclosed defect.[4] In evaluating the integrals around the infinitesimal boundaries C_i, we used the fact that the function $\chi(\mathbf{u}_i+\mathbf{a})$ evaluated on the "rim" of the defect core centered at $\mathbf{u}_i$ and of radius $ae^{V(\mathbf{u}_i)}$ is dominated by a logarithmically diverging contribution due to the ith defect. This leading contribution is approximately constant on C_i. On the other hand, the nondiverging part of $\chi(\mathbf{u}_i+\mathbf{a})$ is multiplied by the perimeter of C_i and hence its contribution is of the order of a. The result of the integration will be insensitive to the orientation of the vectors along the boundary C_i, provided the defect core is small.[5] In this way, we find

$$\oint_{C_i} du^\alpha \gamma_\alpha{}^\beta \chi D_\beta \chi \simeq \chi(\mathbf{u}_i+\mathbf{a}) \oint_{C_i} du^\phi \gamma_\phi{}^r \partial_r \chi \simeq q_i \chi(\mathbf{u}_i+\mathbf{a}). \tag{C17}$$

Upon substituting Eqs. (C17) and (C16) in Eq. (C15), we obtain

$$\begin{aligned} \int_S dA\, D_\alpha(\chi D^\alpha \chi) &= \sum_{i=1}^{N_d} q_i \chi(\mathbf{u}_i+\mathbf{a}) \\ &= \sum_{i=1}^{N_d} q_i V(\mathbf{u}_i) + \sum_{i=1}^{N_d}\sum_{j\neq i}^{N_d} q_i q_j \Gamma(\mathbf{u}_i,\mathbf{u}_j) \\ &\quad + \sum_{i=1}^{N_d} q_i^2 \Gamma(\mathbf{u}_i,\mathbf{u}_i+\mathbf{a}), \end{aligned} \tag{C18}$$

where we used Eq. (C12) to substitute for χ. Substitution of Eq. (C18) and Eq. (C14) in Eq. (C5) then yields

$$\begin{aligned} \frac{F}{K_A} &= F_0 + \sum_{i=1}^{N_d} q_i \left(1 - \frac{q_i}{4\pi}\right) V(r_i) - \sum_{i=1}^{N_d} \frac{q_i{}^2}{8\pi} \ln(a^2) \\ &\quad + \frac{1}{2}\sum_{i=1}^{N_d}\sum_{j\neq i}^{N_d} q_i q_j \Gamma(\mathbf{u}_i,\mathbf{u}_j), \end{aligned} \tag{C19}$$

where we have used Eq. (A15) to evaluate $\Gamma(\mathbf{u}_i,\mathbf{u}_i+\mathbf{a})$. The first term in Eq. (C19) is the free energy of the smooth defect-free texture [see Eq. (17) and preceding discussion]. The free energy difference $\Delta F/K_A$ between a charge neutral defect configuration and a smooth texture thus reads

$$\begin{aligned} \frac{\Delta F(\alpha)}{K_A} &= \frac{1}{2}\sum_{i=1}^{N_d}\sum_{j\neq i}^{N_d} q_i q_j \Gamma_a(r_i,\phi_i,r_j,\phi_j) + \frac{E_c}{K_A}\sum_{i=1}^{N_d} q_i^2 \\ &\quad + \sum_{i=1}^{N_d} q_i \left(1 - \frac{q_i}{4\pi}\right) V(r_i), \end{aligned} \tag{C20}$$

where the subscript a in the Green's function indicates

$$\begin{aligned} \Gamma_a(r_i,\phi_i,r_j,\phi_j) = -\frac{1}{4\pi} \ln\Bigg(&\frac{\Re(r)^2}{a^2} + \frac{\Re(r')^2}{a^2} \\ &- 2\frac{\Re(r)}{a}\frac{\Re(r')}{a}\cos(\phi-\phi')\Bigg). \end{aligned} \tag{C21}$$

In order to absorb the core radius a in the interdefect interaction, we used the elementary algebraic identity

$$\sum_{i=1}^{N_d} q_i^2 = -\sum_{i=1}^{N_d}\sum_{j\neq i}^{N_d} q_i q_j, \tag{C22}$$

valid for charge neutral configurations. The core energy E_c in Eq. (C20) was added by hand and represents short distance physics on scales less than or equal to the core radius. Although the second part of the last term in Eq. (C20) arises as a position-dependent self-energy, it has the same functional form as the geometrical potential discussed in Appendix B, and hence depends on the global shape of the surface.

APPENDIX D: BUMP WITH A BOUNDARY

The aim of this appendix is to study the energetics of a singular vector field on a bumpy surface of circular shape and finite size R. To evaluate the ground state energy in Eq. (C1), we first need to solve the covariant Laplace equation for the bond-angle field $\theta(\mathbf{u})$ in the presence of N_d defects at positions $\mathbf{u}_i$. This is more easily done by switching from $\theta(\mathbf{u})$ to the conjugate field $\chi(\mathbf{u})$, as shown in Eq. (C3), and solving the Poisson equation (C7) satisfied by χ for both free and fixed boundary conditions (see Fig. 18).

The bond-angle field satisfies free boundary conditions if the following relation holds on the circular edge B:

$$\partial_r \theta|_{r=R} = 0, \tag{D1}$$

while for fixed tangential boundary conditions we have

$$\partial_\phi \theta|_{r=R} = 0. \tag{D2}$$

To understand Eq. (D2), recall that we measure the bond angle θ with respect to a rotating basis vector E_r in the radial

[4] The integrated Gaussian curvature in the microscopic disk is vanishingly small.

[5] If the defect core is very large, it may be necessary to place images within the defect core itself to impose a desired boundary condition on its rim. This is not the regime considered in the present work (see Ref. [39] for similar calculations performed in flat space).

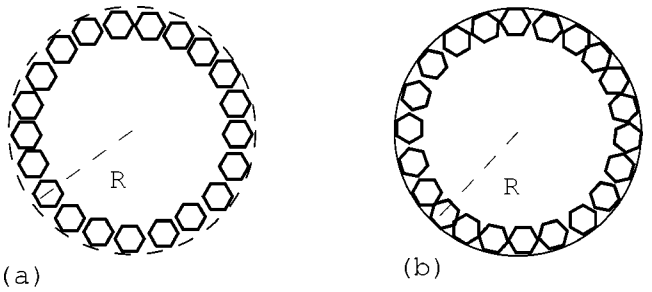

FIG. 18. (a) Schematic illustration of the boundary director texture corresponding to free boundary conditions. The vector order parameter orientation close to the edge of the sample does not vary appreciably as one moves along the radial direction and it is parallel to itself at every point on the boundary. (b) Tangential boundary conditions. The vector order parameter is locally aligned to a wall located at the edge of the sample.

direction. With this convention, θ is equal to a constant when the vector order parameter is aligned with the circular boundary B. We can convert Eqs. (D1) and (D2) into boundary conditions to be satisfied by the conjugate field χ on B. Upon substituting Eq. (D1) in Eq. (C2) and using the fact that A_r is equal to zero, we obtain the constraint that $\chi(\mathbf{u})$ satisfies on B in the case of free boundary conditions:

$$\partial_\phi \chi|_{r=R} = 0. \tag{D3}$$

This corresponds to a Dirichlet problem where $\chi^D(\mathbf{u})$ evaluated on the boundary B assumes an arbitrary constant value c:

$$\chi^D(B) = c. \tag{D4}$$

Upon substituting Eq. (D2) in Eq. (C2), we obtain

$$\partial_r \chi = -\frac{A_\phi}{\gamma_\phi{}^r}, \tag{D5}$$

since $\gamma_\phi^\phi = 0$. Upon substituting Eqs. (B11) and (8) in Eq. (D5) we obtain the boundary condition on χ that corresponds to Eq. (D2):

$$\partial_r \chi^N|_{r=R} = -\frac{1}{R}, \tag{D6}$$

where the superscript indicates that this is a Neumann boundary problem with the normal derivative assuming a constant value.

To solve the Poisson equation (C7) with Neumann or Dirichlet boundary conditions in terms of suitable Green's functions we exploit a covariant version of Green's theorem expressed in terms of two invariant functions of positions $\psi(\mathbf{u})$ and $\varphi(\mathbf{u})$ [40]:

$$\int_S dA[\varphi(\mathbf{u}) D_\alpha D^\alpha \psi(\mathbf{u}) - \psi(\mathbf{u}) D_\alpha D^\alpha \varphi(\mathbf{u})]$$

$$= -\oint_B du^\alpha \gamma_\alpha{}^\beta [\varphi(\mathbf{u}) \partial_\beta \psi(\mathbf{u}) - \psi(\mathbf{u}) \partial_\beta \varphi(\mathbf{u})]. \tag{D7}$$

By applying Eq. (D7) to $\varphi(\mathbf{u}) = \chi(\mathbf{u})$ and $\psi(\mathbf{u}) = \Gamma(\mathbf{u}, \mathbf{u}')$ and using Eqs. (A10) and (C7) we obtain

$$\chi(\mathbf{u}) = \int_S dA' \Gamma(\mathbf{u}', \mathbf{u}) \rho(\mathbf{u}') + \oint_B du'^\alpha \gamma_\alpha{}^\beta \chi(\mathbf{u}') \partial'_\beta \Gamma(\mathbf{u}', \mathbf{u})$$

$$- \oint_B du'^\alpha \gamma_\alpha{}^\beta \Gamma(\mathbf{u}', \mathbf{u}) \partial'_\beta \chi(\mathbf{u}'), \tag{D8}$$

where $\mathbf{u}$ and $\mathbf{u}'$ have been exchanged.[6] The boundary conditions for the Green's function can be conveniently chosen to eliminate unknown quantities in Eq. (D7) as in flat space [41].

For the Dirichlet problem, we choose the Green's function Γ^D so that it vanishes when $\mathbf{u}'$ is on the boundary B:

$$\Gamma^D(B, \mathbf{u}) = 0. \tag{D9}$$

Upon substituting Eq. (D9) in Eq. (D8) and noting that $\chi(\mathbf{u}')$ is constant on the boundary B [see Eq. (D4)], we obtain

$$\chi^D(\mathbf{u}) = \int_S dA' \Gamma^D(\mathbf{u}', \mathbf{u}) \rho(\mathbf{u}')$$

$$+ \chi^D(B) \oint_B du'^\alpha \gamma_\alpha{}^\beta \partial'_\beta \Gamma^D(\mathbf{u}', \mathbf{u}). \tag{D10}$$

The contour integral in the second term of Eq. (D10) corresponds to the flux piercing B which is, in turn, equal to the (unit) charge of the singularity located at $\mathbf{u}$.[7] The final result reads

$$\chi^D(\mathbf{u}) = \int_S dA' \rho(\mathbf{u}') \Gamma^D(\mathbf{u}', \mathbf{u}) + \chi^D(B), \tag{D11}$$

where $\chi^D(B)$ can be set to zero, since the energy in Eq. (C3) is only defined in terms of derivatives of χ. One can check that $\chi^D(\mathbf{u})$ in Eq. (D11) satisfies both the Poisson equation (C7) and the required boundary condition in Eq. (D3). This can be more easily proved by noting that $\Gamma^D(\mathbf{u}', \mathbf{u})$ is symmetric under exchange of its arguments $\mathbf{u}'$ and $\mathbf{u}$.[8]

A similar reasoning applies to $\chi^N(\mathbf{u})$. However, we cannot choose the Green's function so that the second term of Eq. (D8) [which contains the unknown quantity $\chi(\mathbf{u}')$] vanishes.

[6] These manipulations are common in electromagnetism; see, for example, Ref. [41].

[7] This assertion can be proved by applying Stokes theorem [as stated in Eq. (B8) with E_β replaced by $\partial'_\beta \Gamma(\mathbf{u}', \mathbf{u})$] and using Eq. (A10) to evaluate the surface integral.

[8] This assertion can be proved by applying Green's theorem in Eq. (D7) to $\psi(\mathbf{u}) = \Gamma(\mathbf{u}, \mathbf{u}')$ and $\varphi(\mathbf{u}) = \Gamma(\mathbf{u}, \mathbf{u}'')$ and noticing that the right hand side vanishes if the boundary condition in Eq. (D9) is assumed. We can then conclude that $\Gamma^D(\mathbf{u}', \mathbf{u}'') = \Gamma^D(\mathbf{u}'', \mathbf{u}')$ in analogy with familiar results in 3D electrostatics [41].

In fact, by invoking Stokes theorem [see Eq. (B8)], we note that

$$\oint_B du'^{\alpha} \gamma_{\alpha}{}^{\beta} \partial'_{\beta} \Gamma(\mathbf{u}', \mathbf{u}) = 1, \tag{D12}$$

where $\gamma_{\alpha}{}^{\beta}(\mathbf{u}' = B)$ is constant on the circular boundary B and can be brought out of the integral. An appropriate choice of boundary condition on Γ^N that satisfies the constraint in Eq. (D12) is

$$\partial_{r'} \Gamma^N(r', \phi'; r, \phi)|_{r'=R} = \frac{1}{2\pi \gamma_{\alpha}{}^{\beta}(R)} = -\frac{\sqrt{l(R)}}{2\pi R}, \tag{D13}$$

where we used Eq. (B11). The α-dependent function $l(r')$ was defined in Eq. (A4). Note that $l(R) \simeq 1$, for $R \gg r_0$ (see Fig. 2). By substituting Eqs. (D13) and (D6) in Eq. (D8) we obtain

$$\chi^N(\mathbf{u}) = \int_S dA' \Gamma^N(\mathbf{u}', \mathbf{u}) \rho(\mathbf{u}') + \frac{1}{2\pi} \int_0^{2\pi} d\phi' \chi(R, \phi') - \frac{1}{\sqrt{l(R)}} \int_0^{2\pi} d\phi' \Gamma^N(R, \phi'; r, \phi). \tag{D14}$$

The last two integrals are constant and hence can be dropped. We can check explicitly that $\chi^N(\mathbf{u})$ satisfies Eq. (D6) by evaluating the radial derivative of $\chi^N(\mathbf{u})$ in Eq. (D14):

$$\partial_r \chi^N(r, \phi)|_{r=R} = \int_S dA' \rho(\mathbf{u}') \partial_r \Gamma^N(R, \phi'; r, \phi)|_{r=R}, \tag{D15}$$

where the radial derivative of the Green's function assumes the constant value derived in Eq. (D13), provided that $\Gamma^N(\mathbf{u}', \mathbf{u})$ is constructed so that it is symmetric under exchange of its arguments $\mathbf{u}'$ and $\mathbf{u}$ [see Eq. (D19)]. With the aid of Eqs. (C8) and (C12), we obtain

$$\int_S dA' \rho(\mathbf{u}') = \sum_i^{N_d} q_i + 2\pi \left(\frac{1}{\sqrt{l(R)}} - 1 \right). \tag{D16}$$

Upon substituting Eqs. (D16) and (D13) in Eq. (D15), we conclude that the Neumann boundary condition in Eq. (D6) is satisfied provided that

$$\sum_i^{N_d} q_i = 2\pi. \tag{D17}$$

It is reassuring that the topological constraint on the vorticity of the field imposed by the presence of the wall arises as a natural requirement within this formalism. Similarly, the Poisson equation for $\chi^N(\mathbf{u})$ is automatically satisfied.

We are now left with the task of guessing the Green's functions for the Dirichlet and Neumann problems satisfying the boundary conditions in Eqs. (D9) and (D13), respectively. In both cases the Green's function can be determined by the method of images applied in the conformal plane. For every defect with radial coordinate r_i we need an image defect of opposite (equal) topological charge at position r_i' to ensure that Dirichlet's (Neumann) boundary conditions are enforced (see Fig. 19).

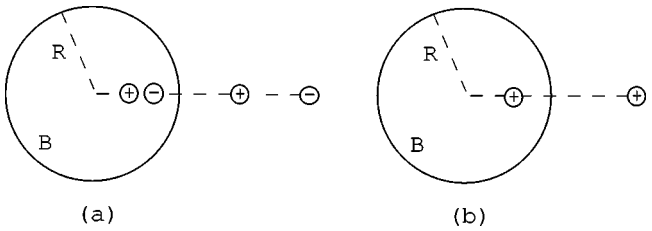

FIG. 19. Schematic illustration of the method of images. The image defect is of the same sign for free boundary conditions (a) and opposite for fixed boundary conditions (b). Defects closer to the center of the circle have images further away from it.

The radial coordinate of the image defect r_i' is determined by the relation

$$\Re(r_i') = \frac{\Re^2(R)}{\Re(r_i)}. \tag{D18}$$

Except for the coordinate change $r \to \Re(r)$, a similar relation arises in elementary electrostatic problems in flat space [35]. A geometric argument that justifies this choice of images in flat space is illustrated in Fig. 20.

Once the position of the source is chosen according to Eq. (D18), we can express the two Green's functions with the concise notation $\Gamma^{D/N}$ as follows:

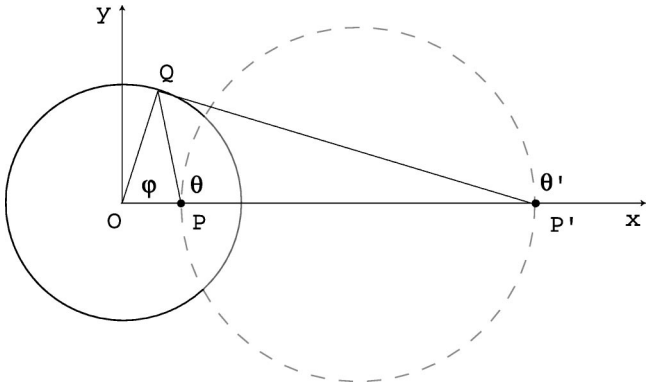

FIG. 20. A topological defect located at position P in a circular domain of radius $\overline{OQ}$ in flat space. Fixed boundary conditions are obtained by placing an image defect of the same sign at a distance $\overline{OP'}$ from the center such that $\overline{OP}\,\overline{OP'} = \overline{OQ}^2$. The two triangles ΔOQP and $\Delta OQP'$ are similar and $\angle OQP = \angle OP'Q = \pi - \theta'$. By the theorem of the external angle, we conclude that $\theta' + \theta = \phi + \pi$ as long as Q lies on the circumference B. This is equivalent to the boundary condition in Eq. (D2) if a nonrotating vector basis is used. Similarly, for free boundary conditions the symmetric Green's function is constant on the boundary if the image defect is negative. Since $\overline{PQ}/\overline{P'Q} = \overline{OP}/\overline{OQ}$, the potential $\ln(\overline{PQ}) - \ln(\overline{P'Q})$ (generated by the defect at distance $\overline{OP}$ and its image) is constant on the circumference of radius $\overline{OQ}$.

$$\Gamma^{D/N}(\mathbf{u},\mathbf{u}') = -\frac{1}{4\pi}\ln[\Re(r)^2+\Re(r')^2-2\Re(r)\Re(r')\times\cos(\phi-\phi')] \pm \frac{1}{4\pi}\ln\left(\Re(r)^2+\frac{\Re(R)^4}{\Re(r')^2}-2\Re(r)\frac{\Re(R)^2}{\Re(r')}\cos(\phi-\phi')\right) \pm f(r'), \tag{D19}$$

where we have introduced a function $f(r')$ to make $\Gamma^{D/N}(\mathbf{u},\mathbf{u}')$ symmetric under exchange of its arguments and to remove a singularity at $r'=0$. Note that we can add $f(r')$ since the defining equation of the Green's function does not contain derivatives of r', only of r:

$$f(r') = \frac{1}{2\pi}\ln\left(\frac{\Re(r')}{\Re(R)}\right). \tag{D20}$$

The plus and minus signs in Eq. (D19) ensure that the Dirichlet and Neumann boundary conditions, respectively, are obeyed. In what follows the sign placed above in the symbols $\pm$ or $\mp$ always indicates the choice suitable for the Dirichlet problem while the one below refers to Neumann boundary conditions. One can explicitly check by substitution that the symmetrized Green's functions $\Gamma^{D/N}(\mathbf{u},\mathbf{u}')$ satisfy the correct boundary conditions, as long as the plus sign is chosen when Γ^D is substituted in Eq. (D9) and the minus sign when Γ^N is substituted in Eq. (D13). Note that, without the extra term $f(r')$ in the expressions for both Green's functions, Γ^D would not be equal to zero on the boundary B and the last term in Eq. (D14) would not be constant when Γ^N is substituted in.

Once the Green's function is obtained, one can readily write down $\chi^{D/N}(\mathbf{u})$ by dropping the constant terms in Eqs. (D11) and (D14):

$$\chi^{D/N}(\mathbf{u}) = \sum_{i=1}^{N_d} q_i\Gamma^{D/N}(\mathbf{u},\mathbf{u}_i) - \int_S dA'\,G(\mathbf{u}')\Gamma^{D/N}(\mathbf{u},\mathbf{u}'). \tag{D21}$$

The Gaussian curvature is given by the covariant Laplacian of the geometric potential introduced in Eq. (B2). Upon integrating by parts twice the second term in Eq. (D21) and applying Stokes theorem repeatedly, we find

$$\chi^{D/N}(\mathbf{u}) = \sum_{i=1}^{N_d} q_i\Gamma^{D/N}(\mathbf{u},\mathbf{u}_i) + V(\mathbf{u}), \tag{D22}$$

where we assume that $R \gg r_0$ so that we can neglect boundary terms. The geometric potential $V(\mathbf{u})$ has the same functional form previously discussed in Appendix B, despite the change in the Green's function.

The evaluation of the energy stored in the field now proceeds along the lines sketched in Appendix C with the only caveat that one needs to choose the appropriate Green's function in Eq. (D19). In the case of Dirichlet boundary conditions one can prove that the boundary integral in Eq. (C16) still vanishes by virtue of the fact that χ is constant on the boundary B and the defect configuration is charge neutral. For the Neumann problem we have

$$\chi^N \oint_B du^\alpha \gamma_\alpha{}^\beta D_\beta \chi^N \approx 4\pi\ln[\Re(R)], \tag{D23}$$

where we assumed that $R \gg r_0$. In this limit $\Re(R)$ is approximately equal to R, as can be checked with the aid of Eqs. (A8) and (A9).

All the remaining intermediate steps to derive the free energy follow as in Appendix C without further assumptions. We can readily generalize Eq. (C20) to evaluate the energy stored in the singular field in the presence of a boundary in the case of both free and fixed boundary conditions. We assume $R \gg r_0$, but the defects do not need to be far away from the boundary. The result is

$$\frac{F^{D/N}}{K_A} = \frac{1}{2}\sum_{j\neq i}^{N_d} q_i q_j \Gamma^{D/N}(x_i;x_j) + F_0 + \sum_{i=1}^{N_d} q_i\left(1-\frac{q_i}{4\pi}\right)V(r_i) + \sum_{i=1}^{N_d}\frac{q_i^2}{4\pi}\ln\left(\frac{\Re(R)}{a}\right) \pm \sum_{i=1}^{N_d}\frac{q_i^2}{4\pi}\ln(1-x_i^2), \tag{D24}$$

where F_0 is defined in Eq. (17). The Green's function expressed in scaled coordinates reads

$$\Gamma^{D/N}(x_i;x_j) = -\frac{1}{4\pi}\ln[x_i^2+x_j^2-2x_ix_j\cos(\phi_i-\phi_j)] \pm \frac{1}{4\pi}\ln[x_i^2x_j^2+1-2x_ix_j\cos(\phi_i-\phi_j)]. \tag{D25}$$

In the case of Neumann boundary conditions, we have suppressed a term diverging like $\ln[\Re(R)]$ associated with the boundary contribution in Eq. (D23). Equation (D25) is expressed in terms of a dimensionless defect position x_i,

$$x_i \equiv \frac{\Re(r_i)}{\Re(R)}. \tag{D26}$$

The plus sign in Eqs. (D25) and (D24) is to be chosen for Dirichlet boundary conditions and the minus sign for Neumann. The last term in Eq. (D24) represents the interaction $U_b^{D/N}(x_i)$ between a single defect located at x_i and the boundary:

$$U_b^{D/N}(x_i) = \pm K_A\sum_{i=1}^{N_d}\frac{q_i^2}{4\pi}\ln(1-x_i^2). \tag{D27}$$

Note that the q-dependent prefactors of $U_b^{D/N}(x_i)$ and the quadratic correction to the curvature interaction [third term in Eq. (D24)] have the same magnitude. This is not a coincidence but a clue to their common origin. As the geometry of

a plane is modified, by either creating a varying curvature or imposing boundaries, the defects experience an additional interaction caused by the conformal transformation of the underlying space. This line of reasoning is powerful and it has been pursued in Ref. [30] to explain some basic features of the interaction between defects and curvature without explicit recourse to the Green's function techniques adopted in this work.

[1] D. R. Nelson and B. I. Halperin, Phys. Rev. B **19**, 2457 (1979).
[2] J. M. Kosterlitz and D. J. Thouless, J. Phys. C **6**, 1181 (1973).
[3] A. P. Young, Phys. Rev. B **19**, 1855 (1979).
[4] C. F. Chou, A. J. Jin, S. W. Hui, C. C. Huang, and J. T. Ho, Science **280**, 1424 (1998).
[5] C. Knobler and R. Desai, Annu. Rev. Phys. Chem. **43**, 207 (1992).
[6] R. Seshadri and R. M. Westervelt, Phys. Rev. Lett. **66**, 2774 (1991).
[7] C. C. Grimes and G. Adams, Phys. Rev. Lett. **42**, 795 (1979).
[8] D. C. Glattli, E. Y. Andrei, and F. I. B. Williams, Phys. Rev. Lett. **60**, 420 (1998).
[9] G. Deville, A. Valdes, E. Y. Andrei, and F. I. B. Williams, Phys. Rev. Lett. **53**, 588 (1984).
[10] C. M. Murray, in *Bond Orientational Order in Condensed Matter Systems*, edited by K. J. Strandburg (Springer, Berlin, 1992).
[11] K. Zahn, R. Lenke, and G. Maret, Phys. Rev. Lett. **82**, 2721 (1999).
[12] R. A. Segalman, A. Hexemer, R. C. Hayward, and E. J. Kramer, Macromolecules **36**, 3272 (2003).
[13] S. Sachdev and D. R. Nelson, J. Phys. C **17**, 5473 (1984).
[14] D. R. Nelson, Phys. Rev. B **28**, 5515 (1983).
[15] D. R. Nelson, *Defects and Geometry in Condensed Matter Physics* (Cambridge University Press, Cambridge, England, 2002).
[16] M. Bowick, D. R. Nelson, and A. Travesset, Phys. Rev. B **62**, 8738 (2000), and references therein.
[17] A. R. Bausch, M. J. Bowick, A. Cacciuto, A. D. Dinsmore, M. F. Hsu, D. R. Nelson, M. G. Nikolaides, A. Travesset, and D. A. Weitz, Science **299**, 1716 (2003).
[18] F. David, E. Guitter, and L. Peliti, J. Phys. (France) **48**, 2059 (1987).
[19] D. R. Nelson and L. Peliti, J. Phys. (France) **48**, 1085 (1987).
[20] E. Guitter and M. Kardar, Europhys. Lett. **13**, 441 (1990).
[21] J. M. Park and T. C. Lubensky, Phys. Rev. E **53**, 2648 (1996).
[22] P. Lenz and D. R. Nelson, Phys. Rev. E **67**, 031502 (2003).
[23] E. Kramer (private communication).
[24] P. G. de Gennes and J. Prost, *The Physics of Liquid Crystals* (Clarendon, Oxford, 1993).
[25] M. Bowick, D. R. Nelson, and A. Travesset, Phys. Rev. E **69**, 041102 (2004).
[26] F. David, in *Statistical Mechanics of Membranes and Surfaces*, edited by D. R. Nelson *et al.* (World Scientific, Singapore, 1989).
[27] D. J. Struik, *Lectures on Classical Differential Geometry* (Dover, New York, 1961).
[28] R. Kamien, Rev. Mod. Phys. **74**, 953 (2002).
[29] T. C. Lubensky and J. Prost, J. Phys. II **2**, 371 (1992).
[30] V. Vitelli and A. M. Turner, e-print cond-mat/0406329.
[31] B. A. Dubrovin, A. T. Fomenko, and S. P. Novikov, *Modern Geometry—Methods and Applications* (Springer, New York, 1992), Vol. 1.
[32] V. I. Smirnov, *A Course of Higher Mathematics* (Pergamon, Oxford, 1964), Vol. 3, Part 2.
[33] A. M. Polyakov, Phys. Lett. **103B**, 307 (1981).
[34] M. Kleman and O. D. Lavrentovich, *Soft Matter Physics* (Springer, New York, 2003).
[35] W. K. H. Panofsky and M. Phillips, *Classical Electricity and Magnetism* (Addison-Wesley, Reading, MA, 1962).
[36] W. F. Vinen, in *Superconductivity*, edited by R. D. Parks (Dekker, New York, 1969), Vol. 2.
[37] G. B. Hess, Phys. Rev. **161**, 189 (1967).
[38] M. Spivak, *A Comprehensive Introduction to Differential Geometry* (Publish or Perish, Berkeley, CA, 1979).
[39] A. Budzin and D. Feinberg, Physica C **235**, 2755 (1994).
[40] A. J. McConnell, *Applications of Tensor Analysis* (Dover, New York, 1957), pp. 184–189.
[41] H. W. Wyld, *Mathematical Methods for Physics* (Perseus, Reading, MA, 1999), pp. 272–276.